This is a preprint, the final version is subject to change, of the American Mineralogist (MSA)
Cite as Authors (Year) Title. American Mineralogist, in press.
DOI: https://doi.org/10.2138/am-2018-6501

Revision 1

Disturbance of the Sm-Nd isotopic system by metasomatic alteration: a case study of fluorapatite from the Sin Quyen Cu-LREE-Au deposit, Vietnam

Xiao-Chun Li[a*], Mei-Fu Zhou[a*], Yue-Heng Yang[b], Xin-Fu Zhao[c], Jian-Feng Gao[d]

a, Department of Earth Sciences, The University of Hong Kong, Hong Kong SAR, China

b, State Key Laboratory of Lithospheric Evolution, Institute of Geology and Geophysics, Chinese Academy of Sciences, Beijing, China

c, State Key Laboratory of Geological Processes and Mineral Resources, and Faculty of Earth Resources, China University of Geosciences, Wuhan 430074, China

d, State Key Laboratory of Ore Deposit Geochemistry, Institute of Geochemistry, Chinese Academy of Sciences, Guiyang 550002, China

*Corresponding author. E-mail: lixiaochun86@gmail.com, mfzhou@hku.hk

Abstract The Neoproterozoic (840 Ma) Sin Quyen deposit in northwestern Vietnam contains replacement Cu-LREE-Au orebodies in Proterozoic metasedimentary rocks. In this deposit, LREE-bearing minerals include allanite-(Ce), monazite-(Ce), chevkinite-(Ce), and fluorapatite. Fluorapatite from orebodies has undergone variable degrees of metasomatic alteration. Samarium-Neodymium isotopic analyses were conducted on altered fluorapatite, and also on allanite-(Ce) and monazite-(Ce), to investigate whether such metasomatism can affect the Sm-Nd isotope system.

Allanite-(Ce) and monazite-(Ce) have $^{147}Sm/^{144}Nd$ ratios ranging from 0.0359 to 0.0549, and $^{143}Nd/^{144}Nd$ ratios from 0.51147 to 0.51172. Their initial $^{143}Nd/^{144}Nd$ values at the time of mineralization range from 0.51126 to 0.51148, but mostly cluster between 0.51135 and 0.51145. Thus, the primary ore-forming fluids were relatively homogeneous in their Sm-Nd isotopic compositions. In the $^{147}Sm/^{144}Nd$ *vs*. $^{143}Nd/^{144}Nd$ diagram, the compositions of allanite-(Ce) and monazite-(Ce) generally plot along a Sm-Nd isochron of 840 Ma, implying that the Sm-Nd isotopic systems of these minerals were either closed or only slightly modified. In contrast, altered fluorapatite crystals have $^{147}Sm/^{144}Nd$ ratios varying from 0.0667 to 0.1348, and $^{143}Nd/^{144}Nd$ ratios from 0.51160 to 0.51199. The calculated initial $^{143}Nd/^{144}Nd$ ratios range widely from 0.51114 to 0.51141, with most values lower than those of the allanite-(Ce) and monazite-(Ce). In the $^{147}Sm/^{144}Nd$ *vs*. $^{143}Nd/^{144}Nd$ diagram, their compositions mostly plot below the 840-Ma Sm-Nd isochron. Petrographic observations and trace elemental analyses show that metasomatic modification of fluorapatite grains led to increases of their Sm/Nd ratios. The unaltered domains in the grains have Sm/Nd ratios varying from 0.114 to 0.200, with an average value of 0.161; whereas the altered domains have Sm/Nd ratios varying from 0.111 to 0.254, with an average value of 0.183. The increased Sm/Nd ratios can cause the calculated initial $^{143}Nd/^{144}Nd$ ratios to be lower than actual initial isotopic ratios, and can also result in compositional deviations from the reference Sm-Nd isochron.

This study demonstrates that the traditionally assumed inert Sm-Nd isotopic system can be metasomatically disturbed due to changes in the Sm/Nd ratio. Therefore, care must be taken when interpreting the Sm-Nd isotopic data from

apatite/apatite-rich rocks that have undergone metasomatic alteration.

Key words: apatite, metasomatic alteration, Sm-Nd isotopes

INTRODUCTION

Apatite is a common accessory mineral in igneous, metamorphic and sedimentary rocks, and hydrothermal ore deposits. Its mineral structure can accommodate a range of trace elements, such as halogens, S, V, As, Sr, and rare earth elements (REE) (Hughes and Rakovan, 2015), which are sensitive to diverse geological processes. Thus, apatite has gained considerable attention as a mineral with many uses within the earth sciences. However, this mineral is susceptible to fluid-induced alteration over a wide range of pressures and temperatures (Harlov, 2015 and references therein), raising questions about the interpretation of its elemental and isotopic composition.

Apatite commonly contains moderate to high concentrations of Sm and Nd. Advances in analytical techniques make it possible to determine the Sm-Nd isotopes of apatite, on a sub-grain scale, by laser ablation multi-collector inductively coupled plasma mass spectrometry (e.g., Fisher et al., 2011; Yang et al., 2014). This approach can provide rapid, texturally sensitive isotopic data, which has many advantages over previous bulk-rock analyses. For example, it allows assessment of Nd isotope equilibrium/disequilibrium among minerals of high-grade metamorphic rocks. Such data are important for understanding Nd isotope exchange during both metamorphism and crustal anatexis processes (Hammerli et al., 2014). Moreover, *in-situ* Sm-Nd isotopic analysis of apatite is important to determine the primary isotopic signature of mantle-derived rocks by analyzing the composition of apatite that directly crystallized from the initial unaffected magmas (Wu et al., 2011, 2013). Apatite is also useful for sediment provenance studies based on its initial Nd isotope composition. Such studies can help unravel the tectonic history of the hinterland and provide insights into the origins and transport pathways of the sediments (e.g., Foster and Carter, 2007; Henderson et al., 2010). It is also notable that apatite is one of the major hosts of Sm

and Nd in many rocks, such as peraluminous and metaluminous granites (Bea, 1996), carbonatites (Chakhmouradian et al., 2017), high-grade metamorphic rocks (Harlov and Forster, 2002; Janots, 2018), and Kiruna-/IOCG-type hydrothermal deposits (Harlov et al., 2002; Schoneveld et al., 2015). This means that the Sm-Nd isotopic composition of apatite can partially or even largely control that of the host rocks. Given the significance of the Sm-Nd isotopic system in apatite, it is necessary to have a proper understanding of the metasomatic effects on the Sm-Nd isotopic changes in any study of apatite. However, to our knowledge, there are only sparse studies concerning this issue.

REE-rich fluorapatite crystals are widespread in the IOCG-type Sin Quyen deposit, northwestern Vietnam, and many crystals have been altered during post-ore metasomatic processes. The altered fluorapatite crystals may record Sm-Nd isotopic changes, and thus provide a good opportunity to study metasomatism-induced isotopic disturbance. In this paper, we present petrographic, elemental, and *in-situ* and bulk-mineral Sm-Nd isotopic data for altered fluorapatite from the Sin Quyen deposit. For comparison, *in-situ* Sm-Nd isotopic data for allanite-(Ce) and monazite-(Ce) from orebodies were also obtained. The comprehensive dataset shows that the Sm-Nd isotopic system of fluorapatite could be variably disturbed during metasomatism, indicating that care must be taken when using Sm-Nd isotopes of altered apatite as geological indicators.

DEPOSIT GEOLOGY

The Sin Quyen deposit is hosted in a metamorphic complex in northwestern Vietnam (Fig. 1a). The protoliths of the metamorphic complex include Archean to Paleoproterozoic igneous intrusions and Paleoproterozoic to Neoproterozoic sedimentary rocks, all of which have been metamorphosed up to amphibolite facies. The metamorphic complex was intruded by Neoproterozoic to Mesozoic plutons, and unconformably covered by Cambrian to Triassic sedimentary rocks (Fig. 1a). Orebodies in the Sin Quyen deposit are distributed along a NW-SE trending zone, about 2.5 km long and 200 to 400 m wide (Fig. 1b). The mining area is divided into

the eastern and western mining districts by the Ngoi Phat River. Exploration in the 1990s showed that this deposit contains 52.8 Mt ore @ 0.91 wt.% Cu, 0.7 wt.% light REE (LREE), and 0.44 g/t Au (McLean 2001).

In this deposit, orebodies are hosted mainly in gneiss and mica-schist. The protoliths of ore-hosting rocks were Neoproterozoic sedimentary rocks (< 920 Ma) (Li et al., 2018b). Individual orebodies are lenses 50 to 600 m long, and 5 to 100 m wide, which extend 50 to 400 m vertically. In a plan view, the orebodies have an overall NW-SE strike, and are generally S-shaped. In cross-sections, they dip at high angles to the northeast or, locally, to the southwest (Fig. 1c). The orebodies consist mainly of massive or banded replacement ores (Fig. 2a), which have experienced variable degrees of post-ore deformation. However, the main ore mineral assemblages and textures have been well-preserved.

Three principle stages of alteration and mineralization have been identified in the Sin Quyen deposit: (I) pre-ore Na alteration; (II) Ca-K alteration and associated Fe-LREE mineralization; and (III) Cu-Au mineralization. Stage I Na alteration is recorded by the formation of hydrothermal albite in orebodies and ore-hosting rocks (Fig. 2b). Minor amounts of magnetite, monazite-(Ce), and chevkinite-(Ce) can also be identified in this stage. Stage II Ca-K alteration is characterized by formation of amphibole and biotite, accompanied by lesser amounts of clinopyroxene, garnet, and titanite. The associated Fe mineralization is represented by abundant magnetite. The LREE mineralization is characterized by abundant allanite-(Ce) and subordinate LREE-rich fluorapatite, monazite-(Ce), and chevkinite-(Ce) (Figs. 2c and d). Stage III Cu-Au mineralization is characterized by deposition of sulfide minerals, mainly chalcopyrite and pyrrhotite, accompanied by subordinate pyrite and gold-bearing phases (Fig. 2e).

Geochronological studies demonstrate that the main mineralization event occurred at ca. 840 Ma (Li et al., 2018b). The orebodies were subsequently intruded by many Neoproterozoic (736-758 Ma) granitic dikes/stocks (Fig. 1c, Li et al., 2018a), and experienced an extensive metamorphic overprint at ca. 30 Ma (Li et al., 2018b). On the basis of alteration mineralogy and isotopic compositions, it was proposed that

149 the mineralization was genetically associated with Neoproterozoic subduction-related
150 magmatic activity (Li et al., 2018b).
151
152 **SAMPLING AND ANALYTICAL METHODS**
153 Fluorapatite is widespread in the orebodies, but varies in abundance from < 1%
154 to > 10%. In this study, four ore samples that contain > 5 vol.% apatite were selected
155 for study. Two samples, SQ13-96 and SQ13-110, were collected from two separate
156 orebodies in the western mining district, and the remaining two samples (LC11-55
157 and LC11-77) were from ore stockpiles of the eastern mining district. The main
158 features of the studied samples are listed in Table 1.
159 Polished thin sections of each sample were investigated first by petrographic
160 microscopy, and then back-scattered electron (BSE) images were obtained using a
161 JEOL JXA-8230 electron microprobe at The University of Hong Kong. Major
162 element compositions of fluorapatite were determined using the same microprobe,
163 following the analytical procedure described by Goldoff et al. (2012). The
164 accelerating voltage was set at 15 kV, the beam current at 20 nA, and the beam
165 diameter at 10 μm. The analyzing crystals were PET (S, P, Ca, Sr, and Cl), LiF (Ce,
166 Fe, and Mn), LDE1 (F), and TAP (As, Si, and Na). The K_α line was chosen for the
167 analyses of S, P, Si, Fe, Mn, Ca, Na, F, and Cl, and the L_α line for As, Ce, and Sr. The
168 counting times on peaks were 10s for F, Cl, Na, and K, and 20 to 40 s for other
169 elements. Background intensities were measured on both sides of the peak for half of
170 the peak time. The standards were lazurite for S and Sr, apatite for P, Ca, and F,
171 gallium arsenide for As, albite for Si and Na, monazite for Ce, magnetite for Fe,
172 rhodonite for Mn, and tugtupite for Cl. All data were corrected using standard ZAF
173 correction procedures. The representative EMPA data are presented in Table 2, and
174 the whole dataset can be found in the Supplementary file.
175 Trace element analyses of fluorapatite were performed using a Geolas Pro
176 193nm laser ablation (LA) system coupled to an Agilent Technologies 7900 type
177 inductively coupled plasma-mass spectrometer (ICP-MS) at the Institute of
178 Geochemistry, Chinese Academy of Sciences. The analyses were performed on thin

sections, with a beam diameter of 32 um and a repetition rate of 4 Hz. The counting times were ~20 s for the background analyses, and ~50 s for the sample analyses. The glass standard NIST 610 was used for external calibration, and was analyzed twice after 8 sample analyses. Calcium was used as the internal standard, and the content of CaO was determined by EMP analyses. The apatite standard Durango was measured as an external standard to monitor the analytical accuracy. Data reduction was performed by the software ICPMSDataCal. The representative LA-ICP-MS trace element data are listed in Table 3, and the whole dataset can be found in the Supplementary file.

In-situ Sm-Nd isotopic analyses were performed using a Neptune multi-collector (MC) ICP-MS, equipped with a Geolas 193 nm excimer laser ablation system at the Institute of Geology and Geophysics, Chinese Academy of Sciences (IGGCAS). The analyses were conducted on thin sections, with a spot size of 90 or 110 μm and a repetition rate of 8 Hz for fluorapatite, a spot size of 20 μm and a repetition rate of 4 Hz for monazite-(Ce), and a spot size of 32 um and a repetition rate of 6 Hz for allanite-(Ce). Each spot analysis involved ~20 s of background data acquisition and ~50 s of data acquisition from the sample. After analyses of eight samples, two standards were analyzed for external calibration. The apatite standard Ap 1 was used for the analyses of fluorapatite (reference values: $^{147}Sm/^{144}Nd = 0.0822 \pm 0.0014$, $^{143}Nd/^{144}Nd = 0.511349 \pm 0.000038$; Yang et al., 2014), and the monazite standard Namaqua was used for the analyses of monazite-(Ce)/allanite-(Ce) (reference values: $^{147}Sm/^{144}Nd = 0.0977 \pm 0.0002$, $^{143}Nd/^{144}Nd = 0.511896 \pm 0.000032$; Liu et al., 2012). The isobaric interference of ^{144}Sm on ^{144}Nd is significant. In order to correct for this interference, we have used the $^{147}Sm/^{149}Sm$ ratio (1.08680) and the measured $^{147}Sm/^{149}Sm$ ratio to calculate the Sm fractionation factor, and then used the measured ^{147}Sm intensity and the natural $^{147}Sm/^{144}Sm$ ratio to estimate the Sm interference on mass 144. The interference-corrected $^{146}Nd/^{144}Nd$ ratio was then normalized to 0.7219 to calculate the Nd fractionation factor. Finally, the $^{143}Nd/^{144}Nd$ and $^{145}Nd/^{144}Nd$ ratios were normalized using the exponential law. The $^{147}Sm/^{144}Nd$ ratio was calculated using the exponential law after correcting for the isobaric interference of

^{144}Sm on ^{144}Nd as described above, and then was externally calibrated against the $^{147}Sm/^{144}Nd$ ratio of the standards. The raw data were exported offline and the whole data-reduction procedure was performed using an in-house Excel VBA (Visual Basic for Applications) macro program. The apatite standard Ap 2 was measured to monitor the analytical accuracy for apatite, yielding weighted mean $^{147}Sm/^{144}Nd$ and $^{143}Nd/^{144}Nd$ ratios of 0.0755 ± 0.0008 and 0.511034 ± 0.000037, respectively, which are consistent, within uncertainty, with the reported values of 0.0764 ± 0.0002 and 0.511007 ± 0.000030, respectively (Yang et al., 2014). The *in-situ* Sm-Nd isotopic data are listed in Table 4.

Bulk-mineral Sm-Nd isotopic compositions of fluorapatite were analyzed at IGGCAS. Fluorapatite crystals were separated from crushed samples using a conventional density separation technique. About 100 mg of fluorapatite was weighed into a 7 ml Savillex^{TM} Teflon beaker, and the appropriate amount of mixed ^{149}Sm-^{150}Nd spike was added. Samples were dissolved in distilled HF + HNO_3 + HBO_3. Chemical separation was performed using a two-stage ion exchange procedure. Firstly, REE were isolated from the matrix elements using a standard cation exchange resin. After that, Sm and Nd were separated using Eichrom LN (LN-C-50B, 100 to 150 μm, 2 ml) chromatographic columns. The Sm-Nd isotopic measurements were conducted using an IsoProbe-T thermal ionization mass spectrometer. The reference material BCR-2 was measured to monitor the accuracy of the entire analytical procedure, with the following results: 6.67 ppm Sm, 28.56 ppm Nd, and $^{143}Nd/^{144}Nd$ = 0.512651 ± 16 (2σ), which are comparable to the reported reference values (Sm: 6.547 ppm, Nd: 28.26 ppm, $^{143}Nd/^{144}Nd$ = 0.512635 ± 29; Jochum et al., 2005). The bulk-mineral Sm-Nd isotopic data are listed in Table 5.

FLUORAPATITE PETROGRAPHY

Fluorapatite occurs as single crystals or aggregates in contact with magnetite, allanite-(Ce), amphibole, biotite and/or garnet of stage II (Figs. 2f and g). Some fluorapatite crystals contain inclusions of magnetite and biotite. Individual fluorapatite crystals are subhedral to anhedral in shape, and have lengths ranging from

50 to 150 μm. Many grains contain intra-crystal fractures, and some have two-phase fluid inclusions (Fig. 2h). The fluid inclusions are commonly distributed along lines, so they are interpreted to have been trapped after crystallization of fluorapatite.

In BSE images, we recognize five textural types of fluorapatite. Type I grains show very faint or concentric growth zoning (Figs. 3a and b). Type II varieties have irregular BSE-bright cores surrounded by darker rims (Fig. 3c). The BSE-dark rims can be either continuous or discontinuous and have variable thicknesses. Boundaries between the BSE-dark and BSE-bright areas may be smooth or irregular. The BSE-bright areas are not homogeneous: some show slightly different levels of gray and some contain small BSE-dark patches. Type III crystals have not only BSE-dark areas along rims but also irregular BSE-dark veins passing through the bright interiors (Fig. 3d). Type IV crystals have a small BSE-bright core or some isolated BSE-bright patches surrounded by relatively wide dark areas (Fig. 3e). These grains grade into homogeneous and relatively dark crystals of Type V (Fig. 3f).

FLUORAPATITE MINERAL COMPOSITION

Major and trace elements

Fluorapatite crystals from the Sin Quyen deposit consist chiefly of CaO and P_2O_5, with 2.39 to 3.71 wt.% F and 0.01 to 1.23 wt.% OH (estimated via charge balance on the halogen site). They also contain minor SiO_2 (below detection limit to 1.01 wt.%), Ce_2O_3 (below detection limit to 1.29 wt.%), SrO (below detection limit to 0.22 wt.%), and FeO (0.01 to 0.64 wt.%). The BSE-bright domains generally have higher contents of Ce_2O_3 and SiO_2 than the BSE-dark domains. Some crystals contain detectable Na_2O (< 0.05 wt.%) and Cl (< 0.02 wt.%).

Different fluorapatite domains contain highly variable (REE + Y) concentrations (319 to 20388 ppm), which correlate positively with Si (Fig. 4a). Thus, the REE^{3+} ions are principally charge-balanced through the coupled substitution $Si^{4+} + (REE+Y)^{3+} = P^{5+} + Ca^{2+}$. It is proposed that in apatite the REE^{3+} ions can also be charge-balanced through the coupled substitution $Na^{+} + (REE+Y)^{3+} = 2Ca^{2+}$ (Roeder et al., 1987; Pan and Fleet, 2002). However, the correlation between (REE + Y) and

Na is not obvious (Fig. 4b), which indicates that the latter coupled substitution is not important for the samples in this study. In each sample, the BSE-dark areas generally have lower (REE+Y) concentrations and higher Sm/Nd ratios than the bright areas (Figs. 5a to d). Trace element analyses were conducted on both BSE-bright and -dark areas of eight fluorapatite crystals. In all crystals, the dark areas have lower (REE+Y) concentrations than the corresponding bright areas. In six of the crystals, the dark area has a higher Sm/Nd ratio than the corresponding bright area, whereas in one crystal, the dark and bright areas have similar Sm/Nd ratios, and in the other, the BSE-dark area has a lower Sm/Nd ratio than the BSE-bright area. Although the BSE-dark domains have lower REE concentrations than the BSE-bright domains, their chondrite-normalized REE patterns are similar, with nearly flat or slightly right/left-inclined profiles from La to Pr, right-inclined profiles from Nd to Dy, and slightly left-inclined to nearly flat profiles from Ho to Lu (Figs. 5e to h). The BSE-dark domains also contain lower amounts of U (21.4 ppm on average), As (49.7 ppm on average), and Ge (9.29 ppm on average) than the BSE-bright domains (63.6 ppm U, 87.5 ppm As, and 24.5 ppm Ge on average).

Sm-Nd isotopes

In-situ Sm-Nd isotopic compositions of fluorapatite were analyzed using large laser spots (90 or 110 μm), so most analyses include mixed BSE-bright and -dark areas. Overall, the analyses yielded scattered $^{147}Sm/^{144}Nd$ (0.0667 to 0.1348) and $^{143}Nd/^{144}Nd$ ratios (0.51160 to 0.51199) (Fig. 6a). Spots containing higher proportions of BSE-bright domains generally have lower $^{147}Sm/^{144}Nd$ ratios than those with higher proportions of BSE-dark domains (Fig. 6a). Bulk-mineral Sm-Nd isotopic analyses of fluorapatite yielded more restricted $^{147}Sm/^{144}Nd$ (0.1024 to 0.1112) and $^{143}Nd/^{144}Nd$ ratios (0.511809 to 0.511822) (Table 5).

Compared with fluorapatite, monazite-(Ce) and allanite-(Ce) have relatively uniform isotopic compositions (Fig. 6a). Monazite-(Ce) has $^{147}Sm/^{144}Nd$ and $^{143}Nd/^{144}Nd$ ratios varying from 0.0375 to 0.0549, and from 0.51157 to 0.51172, respectively. Allanite-(Ce) has $^{147}Sm/^{144}Nd$ and $^{143}Nd/^{144}Nd$ ratios varying from

299 0.0359 to 0.0508, and from 0.51147 to 0.51170, respectively.
300
301 **DISCUSSION**
302
303 *Interpretation of the fluorapatite textures*
304 Most of the fluorapatite crystals, except for those of Type V, show compositional
305 zoning. We note that the development of BSE-dark domains extend from grain rims
306 deep into the interiors. The boundaries between BSE-bright and -dark domains are
307 commonly irregular. Some vein-like BSE-dark domains cut the bright domains. These
308 features imply that fluids played an important role in the formation of the zoned
309 crystals. Therefore, we suggest that the texturally different fluorapatite grains record
310 different degrees of hydrothermal reactions.
311 Original unaltered, REE-rich fluorapatite grains are homogeneous in
312 composition or show primary growth zoning (Type I). During the early stages of
313 alteration, the margins of the fluorapatite began to react with hydrothermal fluids,
314 forming BSE-dark rims surrounding the BSE-bright cores (Type II). Penetration of
315 the fluids into the interiors of fluorapatite formed the irregular BSE-dark veins (Type
316 III). Further alteration led to replacement of most of BSE-bright domains by the
317 BSE-dark domains, leaving only small BSE-bright cores or isolated BSE-bright
318 patches (Type IV). Finally, complete alteration resulted in total replacement of
319 BSE-bright fluorapatite by BSE-dark fluorapatite (Type V).
320
321 *Disturbance of the Sm-Nd isotopic system by metasomatic alteration*
322 Given that many fluorapatite crystals in the Sin Quyen deposit have experienced
323 metasomatic alteration, monazite-(Ce) and allanite-(Ce) from this deposit may also
324 have experienced similar alteration. However, the alteration may not disturb the
325 Sm-Nd isotopic systems of monazite-(Ce) and allanite-(Ce) to large extents, because
326 both phases contain substantially high contents of Sm and Nd. Thus, the initial Sm-Nd
327 isotopic compositions of monazite-(Ce) and allanite-(Ce) could be taken to represent
328 those of the ore-forming fluids. We calculated the initial $^{143}Nd/^{144}Nd$ values of

monazite-(Ce) and allanite-(Ce) at the time of mineralization (840 Ma), and found that they range from 0.51126 to 0.51148, mostly between 0.51135 and 0.51145 (Fig. 6b). Such results indicate that the ore-forming fluids of the Sin Quyen deposit had relatively homogeneous Nd isotopic compositions. Fluorapatite crystals that precipitated from the ore-forming fluids would be expected to have similarly homogeneous Nd isotopic compositions. However, their initial $^{143}Nd/^{144}Nd$ values range widely from 0.51114 to 0.51141, mostly lower than those of monazite-(Ce) and allanite-(Ce) (Fig. 6c). Assuming an initial $^{143}Nd/^{144}Nd$ value of 0.51140 (the average initial $^{143}Nd/^{144}Nd$ value of monazite-(Ce) and allanite-(Ce)), a reference isochron with an age of 840 Ma is shown in the $^{147}Sm/^{144}Nd$ *vs*. $^{143}Nd/^{144}Nd$ diagram (Fig. 6a). In this diagram, the compositions of most analyzed fluorapatites, especially grains with higher proportions of BSE-dark (altered) domains, plot below the reference isochron (Fig. 6a), indicating that the Sm-Nd isotopic system was disturbed during the post-ore metasomatic process.

Disturbance of the Sm-Nd isotopic system could potentially be due to: (1) change(s) in the $^{143}Nd/^{144}Nd$ ratio; (2) change(s) in the $^{147}Sm/^{144}Nd$ ratio; or (3) a combination of (1) and (2). If the metasomatic fluids had $^{143}Nd/^{144}Nd$ ratios different from those of unaltered fluorapatite, the $^{143}Nd/^{144}Nd$ ratios of fluorapatite could have been changed, because Nd can be introduced into fluorapatite from the fluids. However, it is difficult to determine how much Nd was gained from metasomatic fluid. The accurate isotopic composition of metasomatic fluid is not known. Thus, it cannot be certain if the disturbance of Sm-Nd isotopic system was mainly due to the changes in the $^{143}Nd/^{144}Nd$ ratios. Variable removal of Nd from fluorapatite during metasomatism may imply insignificant gain of Nd from the fluid. Thus, the $^{143}Nd/^{144}Nd$ ratio of fluorapatite may not be changed significantly.

Our analyses show that the Sm/Nd ratios of fluorapatite commonly increased during metasomatism, although in rare crystals the ratios decreased. If the Sm/Nd ratios were increased immediately after the formation of fluorapatite, the compositions of altered domains would evolve along new paths, but their present-day compositions, together with those of unaltered domains, would still lie on the 840-Ma

isochron (Fig. 7a). If the Sm/Nd ratios increased at some later time, the compositional evolutionary paths of the altered domains would be more complex, as graphically illustrated in the $^{147}Sm/^{144}Nd$ *vs*. $^{143}Nd/^{144}Nd$ diagram (Fig. 7b). At t_0, the initial composition of an unaltered fluorapatite crystal could have been located at Point b_0. As time passed, its composition would have evolved along path b_0-b_1. If the crystal was altered at t_1, its Sm/Nd ratio could have been increased to Point b_1'. From then on, the composition of the altered fluorapatite would evolve along a new path, but the question is where the new path would stop. To help answer this question, we have inserted point d_1 on the reference isochron with an age of (t_0-t_1). This point has the same $^{147}Sm/^{144}Nd$ ratio as Point b_1', but its $^{143}Nd/^{144}Nd$ ratio is higher. Assuming that the Sm-Nd isotopic system of Point d_1 remained closed since t_1, the composition of this point would just intersect with the reference isochron of 840 Ma at the present day (Point d_p). Because Points b_1' and d_1 have the same $^{147}Sm/^{144}Nd$ ratio, the increases in the $^{143}Nd/^{144}Nd$ ratio at the time interval of t_1 to the present day should be the same for the two points. Since Point b_1' has a $^{143}Nd/^{144}Nd$ ratio lower than that of Point d_1, the path b_1'- b_p' cannot intersect with the isochron of 840 Ma, i.e., the present-day composition of the altered fluorapatite must be plotted below the 840-Ma isochron.

To obtain the initial $^{143}Nd/^{144}Nd$ ratio of the altered fluorapatite, two evolution paths need to be traced backward (Fig. 7c). To obtain the $^{143}Nd/^{144}Nd$ ratio at t_1, path b_p'- b_1' needs to be traced backward. The mathematical equation can be expressed as:

$$(^{143}Nd/^{144}Nd)_{t1} = (^{143}Nd/^{144}Nd)_p - (^{147}Sm/^{144}Nd)_p\,(e^{\lambda t1}-1) \quad \textbf{(1)}$$

where $(^{143}Nd/^{144}Nd)_p$ denotes the present-day $^{143}Nd/^{144}Nd$ ratio, $(^{147}Sm/^{144}Nd)_p$ denotes the present-day $^{147}Sm/^{144}Nd$ ratio, and λ is the decay constant of ^{147}Sm.

To further obtain the $^{143}Nd/^{144}Nd$ ratio at t_0, path b_1-b_0 also needs to be traced backward using the mathematical expression:

$$(^{143}Nd/^{144}Nd)_{t0} = (^{143}Nd/^{144}Nd)_{t1} - (^{147}Sm/^{144}Nd)_{unchanged}\,[e^{\lambda(t0-t1)} - 1] \quad \textbf{(2)}$$

where $(^{147}Sm/^{144}Nd)_{unchanged}$ denotes the $^{147}Sm/^{144}Nd$ ratio before the metasomatic alteration at t_1.

Substitute equation (1) into equation (2):

$$(^{143}Nd/^{144}Nd)_{t0} = (^{143}Nd/^{144}Nd)_{p} - (^{147}Sm/^{144}Nd)_{p}\,(e^{\lambda * t1} - 1) - {}^{147}Sm/^{144}Nd_{unchanged} * [e^{\lambda(t0-t1)} - 1], \quad \textbf{(3)}$$

The initial $^{143}Nd/^{144}Nd$ ratio of the altered apatite can be obtained.

If the alteration-induced change of the $^{147}Sm/^{144}Nd$ ratio is ignored, one evolutionary path (b_p'- b_{cal}) or two continuous evolutionary paths (b_p'- b_1' and b_1'-b_{cal}) need to be traced backward (Fig. 7d). The mathematical expression is:

$$(^{143}Nd/^{144}Nd)_{cal} = (^{143}Nd/^{144}Nd)_{p} - (^{147}Sm/^{144}Nd)_{p}\,(e^{\lambda * t1} - 1) - {}^{147}Sm/^{144}Nd_{changed} * [e^{\lambda(t0-t1)} - 1] \quad \textbf{(4)}$$

where $(^{147}Sm/^{144}Nd)_{changed}$ denotes the $^{147}Sm/^{144}Nd$ ratio after the metasomatic alteration at t_1.

It is obvious that the ratio obtained from equation (4) will be smaller than that obtained from equation (3), because $(^{147}Sm/^{144}Nd)_{changed}$ is larger than $(^{147}Sm/^{144}Nd)_{unchanged}$.

The above illustrations demonstrate that an increase in the Sm/Nd ratio can cause the present-day composition of the altered apatite to plot below the present-day Sm-Nd isochron, and can also cause the calculated initial $^{143}Nd/^{144}Nd$ ratio to be lower than the actual initial isotopic ratio. Here we want to point out that fluorapatite from the Sin Quyen deposit may have experienced multiple stages of metasomatic alteration, during which the Sm/Nd ratios may have been increased and/or even decreased several times. Thus, here we present only a simple and ideal illustration of the change in the Sm-Nd isotope system. It is also notable that, although the

419 increase(s) in the Sm/Nd ratios can explain the observed Sm-Nd isotopic disturbances,
420 it does not mean that this is the only possible cause. Addition of Nd from
421 compositionally different fluids might also induce somewhat changes in $^{143}Nd/^{144}Nd$
422 ratios, and more studies are needed to test this possibility.
423

424 **IMPLICATION**

425 Previous experimental studies have demonstrated that apatite can be altered by a
426 variety of fluids, including aqueous brines ($NaCl$-KCl-$CaCl_2$-H_2O), H_2O-CO_2 aqueous
427 fluids, and low pH acidic fluids, over a wide range of temperatures (300-900 ^oC) and
428 pressures (500-1000 MPa) (Harlov et al., 2002b, 2005; Harlov and Förster, 2003). In
429 addition to laboratory experiments, apatite from a wide range of natural rocks has also
430 been found to experience metasomatic alteration (Harlov, 2015 and references
431 therein). Previous studies concerned mainly on the elemental changes during
432 metasomatic alteration of apatite (e.g., Harlov et al., 2002a; Bonyadi et al., 2011; Li
433 and Zhou, 2015; Heidarian et al., 2018), but much less on the alteration-induced
434 Sm-Nd isotopic disturbance.

435 It has long been assumed that Sm and Nd have very similar chemical behaviors,
436 and thus the Sm/Nd ratios are little affected by hydrothermal alteration (White, 2014).
437 However, this study demonstrates that Sm/Nd ratios can obviously be changed during
438 metasomatic alteration, and that this change will affect the evolution of the Sm-Nd
439 isotopic system. Similar results have also been documented in other studies. For
440 example, apatite crystals from magnetite-apatite ores in the Kiruna area, Sweden, also
441 experienced metasomatic alteration, and the alteration induced variable REE removal
442 (Harlov et al., 2002a). The unaltered REE-rich apatite domains have an average
443 Sm/Nd ratio of 0.16, whereas the altered REE-poor domains have an average ratio of
444 0.21. Similarly, unaltered REE-rich apatite crystals from magnetite ores in the Bafq
445 District, Iran, have Sm/Nd ratios ranging from 0.13 to 0.22, whereas altered,
446 REE-poor crystals have ratios ranging from 0.18 to 0.55 (Stosch et al., 2011). It has
447 also been found that unaltered, REE-rich fluorapatite domains, from the Yinachang
448 Fe-Cu-(LREE) deposit, southwestern China, have Sm/Nd ratios ranging from 0.14 to

449 0.25, whereas altered, REE-poor domains have ratios ranging from 0.19 to 0.45 (Li
450 and Zhou, 2015). These examples indicate that REE loss is a common process during
451 metasomatic alteration of apatite, and the removal of Sm is usually less than the
452 removal of Nd, resulting in an increase in the Sm/Nd ratio. This less removal of Sm
453 may be partially related to its higher compatibility in the apatite structure, as
454 demonstrated in previous apatite-melt REE partition experiments (Watson and Green,
455 1981; Klemme and Dalpe, 2003; Prowatke and Klemme, 2006). It is also notable that
456 experimental studies demonstrate that, at elevated temperatures (> 150 ^{o}C), $NdCl^{2+}$
457 and NdF^{2+} species in hydrothermal solutions are more stable than $SmCl^{2+}$ and SmF^{2+}
458 species, respectively (Migdisov and Williams-Jones, 2009). Since Cl and F are two
459 major anion ligands in most upper crustal fluids (Yardly, 2012), the removal of
460 smaller amounts of Sm relative to Nd may also be related to the predominance of Cl^{-}
461 and/or F^{-} in the metasomatic fluids.

462 In addition to the Sm-Nd isotopic system, it has been documented that Sr and O
463 isotopes of apatite can also be modified during metasomatic alteration. For example,
464 the unaltered fluorapatite crystals from the Taocun iron-oxide apatite deposit, eastern
465 China, have $^{87}Sr/^{86}Sr$ ratios ranging from 0.7077 to 0.7087, and $\delta^{18}O$ values ranging
466 from +5.3 to +7.5‰. After reacting with upper crustal meteoric water, the fluorapatite
467 crystals have obviously higher $^{87}Sr/^{86}Sr$ ratios (0.7083-0.7097) and lower $\delta^{18}O$ values
468 (-3.0 to +3.4‰) (Zeng et al., 2016).

469 In summary, if metasomatism occurs, bulk-rock isotopic compositions of
470 apatite/apatite-rich rocks may show mixed signatures, and hence be geologically
471 misleading. Therefore, it is important to evaluate the effects of metasomatic alteration
472 on mineral textures and mineral chemistry before using apatite as a geological
473 indicator.

474

475 **Acknowledgements**

476 We would like to express our great thanks to Dr. Tingguang Lan for his
477 assistance with trace element analyses, and Dr. Chang Zhang for his assistance with
478 in-situ Sm-Nd isotopic analyses. Prof. Paul T. Robinson is greatly appreciated for

useful discussion and language polishing. Prof. Daniel E. Harlov and an anonymous reviewer are greatly appreciated for their constructive reviews. Dr. Fangzhen Teng is gratefully acknowledged for his editorial handling. This study was supported by NSFC grants (41473038, 41472068, 41525012), and the "CAS Hundred Talents" Project to Jian-Feng Gao.

References

Bea, F. (1996) Residence of REE, Y, Th and U in granites and crustal protoliths: implications for the chemistry of crustal melts. Journal of petrology, 37, 521-552.

Chakhmouradian, A.R., Reguir, E.P., Zaitsev, A.N., Coueslan, C., Xu, C., Kynicky, J., Mumin, A.H., and Yang, P. (2017) Apatite in carbonatitic rocks: Compositional variation, zoning, element partitioning and petrogenetic significance. Lithos, 274-275, 188-213.

Fisher, C.M., McFarlane, C.R.M., Hanchar, J.M., Schmitz, M.D., Sylvester, P.J., Lam, R., and Longerich, H.P. (2011) Sm-Nd isotope systematics by laser ablation-multicollector-inductively coupled plasma mass spectrometry: Methods and potential natural and synthetic reference materials. Chemical Geology, 284, 1-20.

Foster, G.L., and Carter, A. (2007) Insights into the patterns and locations of erosion in the Himalaya - A combined fission-track and in situ Sm-Nd isotopic study of detrital apatite. Earth and Planetary Science Letters, 257, 407-418.

Goldoff, B., Webster, J.D., and Harlov, D.E. (2012) Characterization of fluor-chlorapatites by electron probe microanalysis with a focus on time-dependent intensity variation of halogens. American Mieneralogist, 97, 1103-1115.

Hammerli, J., Kemp, A.I.S., and Spandler, C. (2014) Neodymium isotope equilibration during crustal metamorphism revealed by in situ microanalysis of REE-rich accessory minerals. Earth and Planetary Science Letters, 392, 133-142.

Harlov, D.E., and Förster, H.J. (2002) High-grade fluid metasomatism on both a local and regional scale: the Seward Peninsula, Alaska and the Val Strona di Omegna, Ivrea-Verbano zone, northern Italy. Part II: Phosphate mineral chemistry. Journal

509 of Petrology, 43, 801-824.
510 Harlov, D.E., Andersson, U.B., Förster, H.J., Nyström, J.O., Dulski, P., and Broman,
511 C. (2002a) Apatite-monazite relations in the Kiirunavaara magnetite-apatite ore,
512 northern Sweden. Chemical Geology, 191, 47-72.
513 Harlov, D.E., Förster, H.J. and Nijland, T.G. (2002b) Fluid-induced nucleation of
514 REE-phosphate minerals in apatite: nature and experiment. Part I. Chlorapatite.
515 American Mineralogist, 87, 245-261.
516 Harlov, D.E., and Förster, H.J. (2003) Fluid-induced nucleation of REE phosphate
517 minerals in apatite: nature and experiment. Part II. Fluorapatite. American
518 Mineralogist, 88, 1209-1229.
519 Harlov, D.E., Wirth, R., and Förster, H.J. (2005) An experimental study of
520 dissolution-reprecipitation in fluorapatite: fluid infiltration and the formation of
521 monazite. Contribution to Mineralogy and Petrology, 150, 268-286.
522 Harlov, D.E. (2015) Apatite: a fingerprint for metasomatic processses. Elements, 11,
523 171-176.
524 Heidarian, H.., Lentz, D.R., Alirezaei, S., McFarlane, C.R.M., Peighambari, S. (2018)
525 Multiple Stage Ore Formation in the Chadormalu Iron Deposit, Bafq Metallogenic
526 Province, Central Iran: Evidence from BSE Imaging and Apatite EPMA and
527 LA-ICP-MS U-Pb Geochronology. Minerals, 8, 87.
528 Henderson, A.L., Foster, G.L., and Najman, Y. (2010) Testing the application of in
529 situ Sm-Nd isotopic analysis on detrital apatites: A provenance tool for constraining
530 the timing of India-Eurasia collision. Earth and Planetary Science Letters, 297,
531 42-49.
532 Hughes, J.M., and Rakovan, J.F. (2015) Structurally robust, chemically diverse:
533 apatite and apatite supergroup minerals. Elements, 11, 165-170.
534 Janots, E., Austrheim, H., Spandler, C., Hammerli, J., Trepmann, C.A., Berndt, J.,
535 Magnin, V., and Kemp, A. (2018) Rare earth elements and Sm-Nd isotope
536 redistribution in apatite and accessory minerals in retrogressed lower crust material
537 (Bergen Arcs, Norway). Chemical Geology, in press.

538 Jochum, K.P., Nohl, U., Herwig, K., Lammel, E., Stoll, B., and Hofmann, A.W. (2005)
539 GeoReM: A New Geochemical Database for Reference Materials and Isotopic
540 Standards. Geostandards and Geoanalytical Research, 29, 333-338.
541 Klemme, S., and Dalpe, C. (2003) Trace-element partitioning between apatite and
542 carbonatite melt. American Mineralogist, 88, 639-646.
543 Li, X.C., and Zhou, M.F. (2015) Multiple stages of hydrothermal REE remobilization
544 recorded in fluorapatite in the Paleoproterozoic Yinachang Fe-Cu-(REE) deposit,
545 Southwest China. Geochimica et Cosmochimica Acta, 166, 53-73.
546 Li, X.C., and Zhou, M.F. (2017) Hydrothermal alteration of monazite-(Ce) and
547 chevkinite-(Ce) from the Sin Quyen Fe-Cu-LREE-Au deposit, northwestern
548 Vietnam. American Mineralogist, 102, 1525-1541.
549 Li, X.C., Zhao, J.H., Zhou, M.F., Gao, J.F., Sun, W.H., and Tran, M.D. (2018a)
550 Neoproterozoic granitoids from the Phan Si Pan belt, Northwest Vietnam:
551 Implication for the tectonic linkage between Northwest Vietnam and the Yangtze
552 Block. Precambrian Research, 209, 212-230.
553 Li, X.C., Zhou, M.F., Chen, W.T., Zhao, X.F., and Tran, M.D. (2018b) Uranium-lead
554 dating of hydrothermal zircon and monazite from the Sin Quyen
555 Fe-Cu-REE-Au-(U) deposit, northwestern Vietnam. Mineralium Deposita, 53,
556 399-416.
557 Liu, Z.C., Wu, F.Y., Yang, Y.H., Yang, J.H., and Wilde, S.A. (2012) Neodymium
558 isotopic compositions of the standard monazites used in U-Th-Pb geochronology.
559 Chemical Geology, 334, 221-239.
560 McLean, R.N. (2001) The Sin Quyen iron oxide-copper-gold-rare earth oxide
561 mineralization of North Vietnam, in Porter, T.M., e.d., Hydrothermal iron oxide
562 copper–gold & related deposits: a global perspective, volume 2: Adelaide, PGC
563 Publishing, p.293-301.
564 Migdisov, A.A., Williams-Jones, A.E., and Wagner, T. (2009) An experimental study
565 of the solubility and speciation of the Rare Earth Elements (III) in fluoride- and
566 chloride-bearing aqueous solutions at temperatures up to 300°C. Geochim
567 Cosmochim Acta, 73, 7087-7109.

568 Pan, Y., and Fleet, M.E. (2002) Composition of the apatite-group minerals:
569 substitution mechanisms and controlling factors. In: Kohn MJ, Rakovan J, Hughes
570 JM (eds) Phosphates: geochemical, geobiological, and materials importance, 48,
571 13–49.
572 Prowatke, S., and Klemme, S. (2006) Trace element partitioning between apatite and
573 silicate melts. Geochimica et Cosmochimica Acta, 70, 4513-4527.
574 Roeder, P.L., MacArthur, D., Ma, X.P., Palmer, G.R., and Mariano, A.N. (1987)
575 Cathodoluminescence and microprobe study of rare-earth elements in apatite.
576 American Mineralogist, 72, 801-811.
577 Schoneveld, L., Spandler, C., and Hussey, K. (2015) Genesis of the central zone of
578 the Nolans Bore rare earth element deposit, Northern Territory, Australia.
579 Contribution to Mineralogy and Petrology, 170, 11.
580 Stosch, H.G., Romer, R.L., Daliran, F., and Rhede, D. (2011) Uranium-lead ages of
581 apatite from iron oxide ores of the Bafq District, East-Central Iran. Mineralium
582 Deposita, 46, 9-21.
583 Ta, V.D. et al. (1975) The geological report on detailed exploration of the Sin Quyen
584 copper deposit. General Department of Geology, Hanoi (unpublished).
585 Watson, E.B., and Green, T.H. (1981) Apatite/liquid partition coefficients for the
586 rare-earth elements and strontium. Earth and Planetary Science Letters 56, 405-421.
587 White W.M. 2014. Isotope Geochemistry. Wiley. 498p.
588 Wu, F.Y., Yang, Y.H., Li, Q.L. Mitchell, R.H., Dawson, J.B., Brandl, G., and Yuhara,
589 M. (2011) In-situ determination of U–Pb ages and Sr–Nd–Hf isotopic constraints
590 on the petrogenesis of the Phalaborwa carbonatite Complex, South Africa. Lithos,
591 127, 309-322.
592 Wu, F.Y., Arzamastsev, A.A., Mitchell, R.H., Li, Q.L., Sun, J., Yang, Y.H., and
593 Wang, R.C. (2013) Emplacement age and Sr–Nd isotopic compositions of the
594 Afrikanda alkaline ultramafic complex, Kola Peninsula, Russia. Chemical Geology,
595 353, 210-229.
596 Yang, Y.H., Wu, F.Y., Yang, J.H., Chew, D.M., Xie, L.W., Chu, Z.Y., Zhang, Y.B.,

597 and Huang, C. (2014) Sr and Nd isotopic compositions of apatite reference
598 materials used in U-Th-Pb geochronology. Chemical Geology, 385, 35-55.
599 Yardley, B.W.D. (2012) The chemical composition of metasomatic fluids in the crust,
600 in Harlov, D.E., and Austrheim H., e.d., Metasomatism and the chemical
601 transformation of rock, Springer, p. 17-53.
602 Zeng, L.P., Zhao, X.F., Li, X.C., Hu, H., and McFarlane, C. (2016) In situ elemental
603 and isotopic analysis of fluorapatite from the Taocun magnetite-apatite deposit,
604 Eastern China: Constraints on fluid metasomatism. American Mineralogist, 101,
605 2468-2483.
606

607 **Figure captions**

608

609 Fig. 1 (a) Geological map of the northwestern Vietnam region. (b) Simplified
610 geological map of the Sin Quyen deposit (modified from Ta et al. 1975). (c) Cross
611 section A-B located in (a), showing the distribution of orebodies (modified from
612 McLean 2001).
613

614 Fig. 2 (a) A sample of banded ore, which mainly contains magnetite- and
615 chalcopyrite-rich bands. (b) Stage I albite crystals overprinted by later-stage
616 amphibole and biotite. (c) Typical mineral assemblage of stage II (magnetite +
617 allanite-(Ce) + amphibole + biotite). (d) Monazite-(Ce) crystals in ore sample. (e)
618 Stage III sulfide minerals overprinting earlier stage minerals. (f) Individual
619 fluorapatite crystals in contact with magnetite, and biotite. (g) Fluorapatite aggregates
620 in contact with allanite-(Ce) and magnetite. (h) Two-phase fluid inclusions in
621 fluorapatite. Mineral abbreviations: Aln-allanite-(Ce), Amp-amphibole,
622 Ap-fluorapatite, Bt-biotite, Ccp-chalcopyrite, Mag-magnetite, Mnz-monazite-(Ce),
623 Po-pyrrhotite, Qz-quartz.
624

625 Fig. 3 (a) A fluorapatite crystal with very faint zoning. (b) A fluorapatite crystal with
626 concentric growth zoning. Note that this crystal has discontinuous dark areas along

627 the grain rim. (c) Fluorapatite crystals with dark rims of varying thickness around the
628 bright cores. (d) A fluorapatite crystal with dark veins crossing the bright interior. (e)
629 A fluorapatite crystal with small bright patches surrounded by dark area. (f)
630 Homogeneous, dark fluorapatite crystals. Mineral abbreviations are the same as those
631 in Fig. 2.
632
633 Fig. 4 Plots of Si *vs*. (REE+Y) and Na *vs.* (REE+Y) concentrations for fluorapatite.
634
635 Fig. 5 (a) to (d) Plots of (REE+Y) *vs*. Sm/Nd for fluorapatite from the samples in this
636 study. (e) to (h) Chondrite-normalized REE profiles for fluorapatite from studied
637 samples.
638
639 Fig. 6 (a) Plot of $^{143}Nd/^{144}Nd$ *vs.* $^{147}Sm/^{144}Nd$ for fluorapatite, allanite-(Ce), and
640 monazite-(Ce). A Sm-Nd isochron of 840 Ma is shown for reference. (b) Histogram
641 showing initial $^{143}Nd/^{144}$ Nd ratios of allanite-(Ce) and monazite-(Ce). (c) Histogram
642 showing initial $^{143}Nd/^{144}$ Nd ratios of fluorapatite.
643
644 Fig. 7 $^{147}Sm/^{144}Nd$ *vs*. $^{143}Nd/^{144}Nd$ diagrams illustrating: (a) and (b) the effect of the
645 Sm/Nd ratio change on the evolution of the Sm-Nd isotopic system, (c) methodology
646 regarding the back tracing of the initial isotopic composition of a sample that has
647 experienced a Sm/Nd ratio change, and (d) how to back trace the initial isotopic
648 composition of a sample if the change in the Sm/Nd ratio is ignored. See the text for
649 further discussion.

(a)

N

103°40′

0 10km

22°40′

22°30′

100°E 103°E 106°E

25°N

23°N

21°N

N

200km

China

Vietnam

Laos

Hanoi

Sin Quyen deposit

China

Vietnam

Lao Cai

Phanerozoic strata

Permian felsic intrusion

Permian volcanic rock

Proterozoic metamorphic complex

Neoproterozoic felsic intrusion

Fault

(b)

Sin Quyen Fault

Ngoi Phat River

B

A

N

0 200 400m

(c)

A

B

+100m

0m

-100m

-200m

Proterozoic metapelite

Phanerozoic strata

Orebody

Alteration halo

Fig. 1


(a)

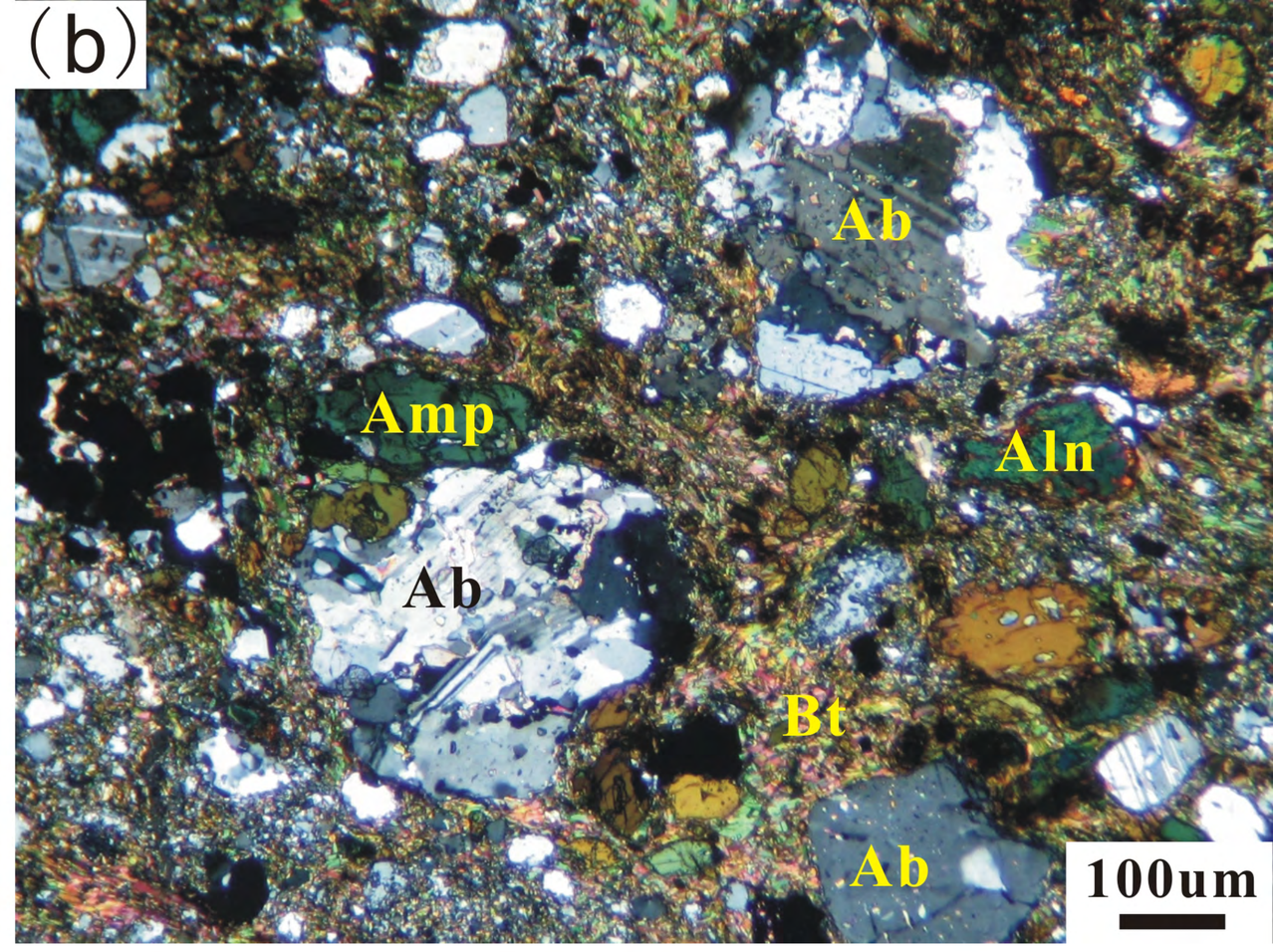
(b)
Ab
Amp
Aln
Ab
Bt
Ab
100um

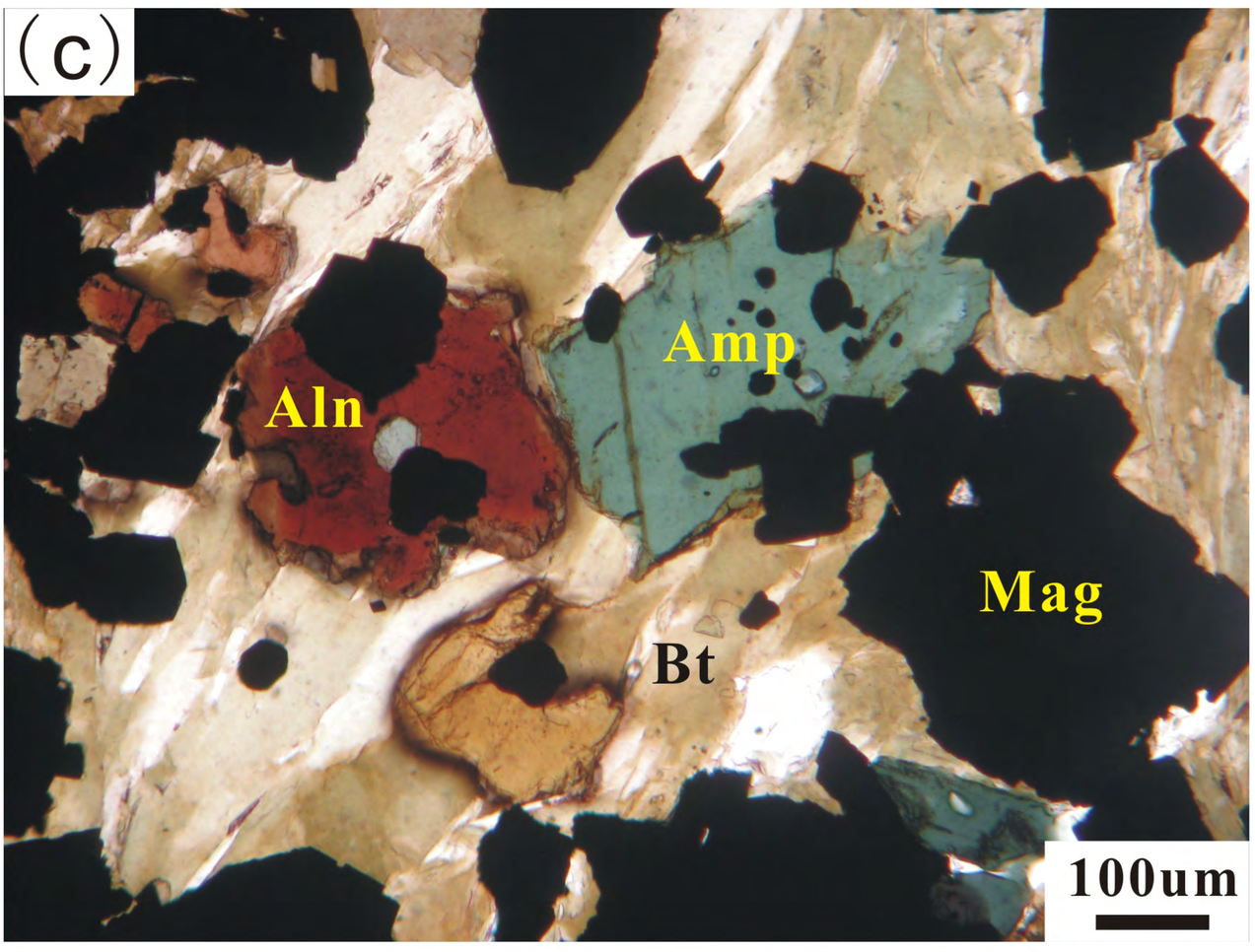
(c)
Aln
Amp
Mag
Bt
100um

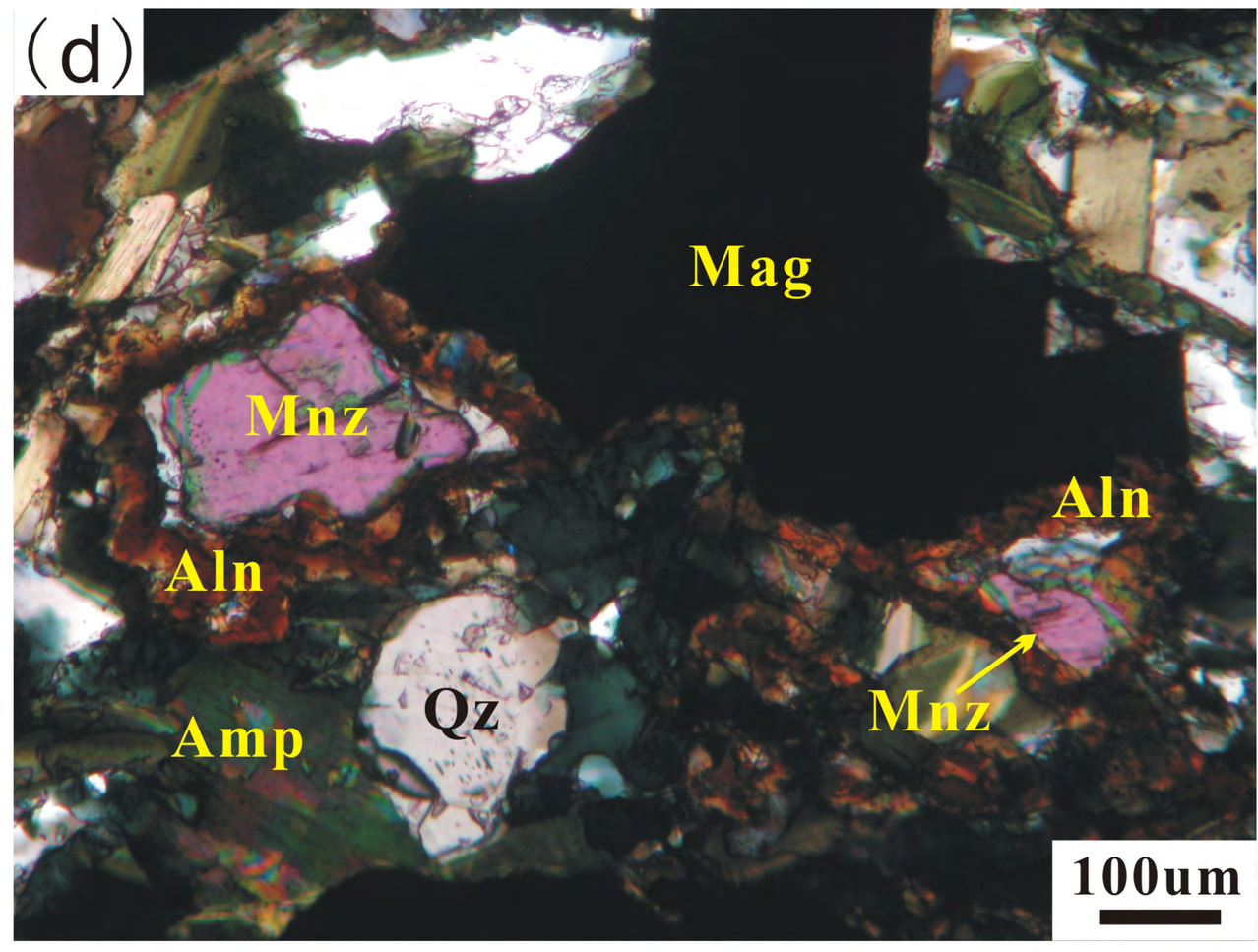
(d)
Mag
Mnz
Aln
Aln
Qz
Amp
Mnz
100um

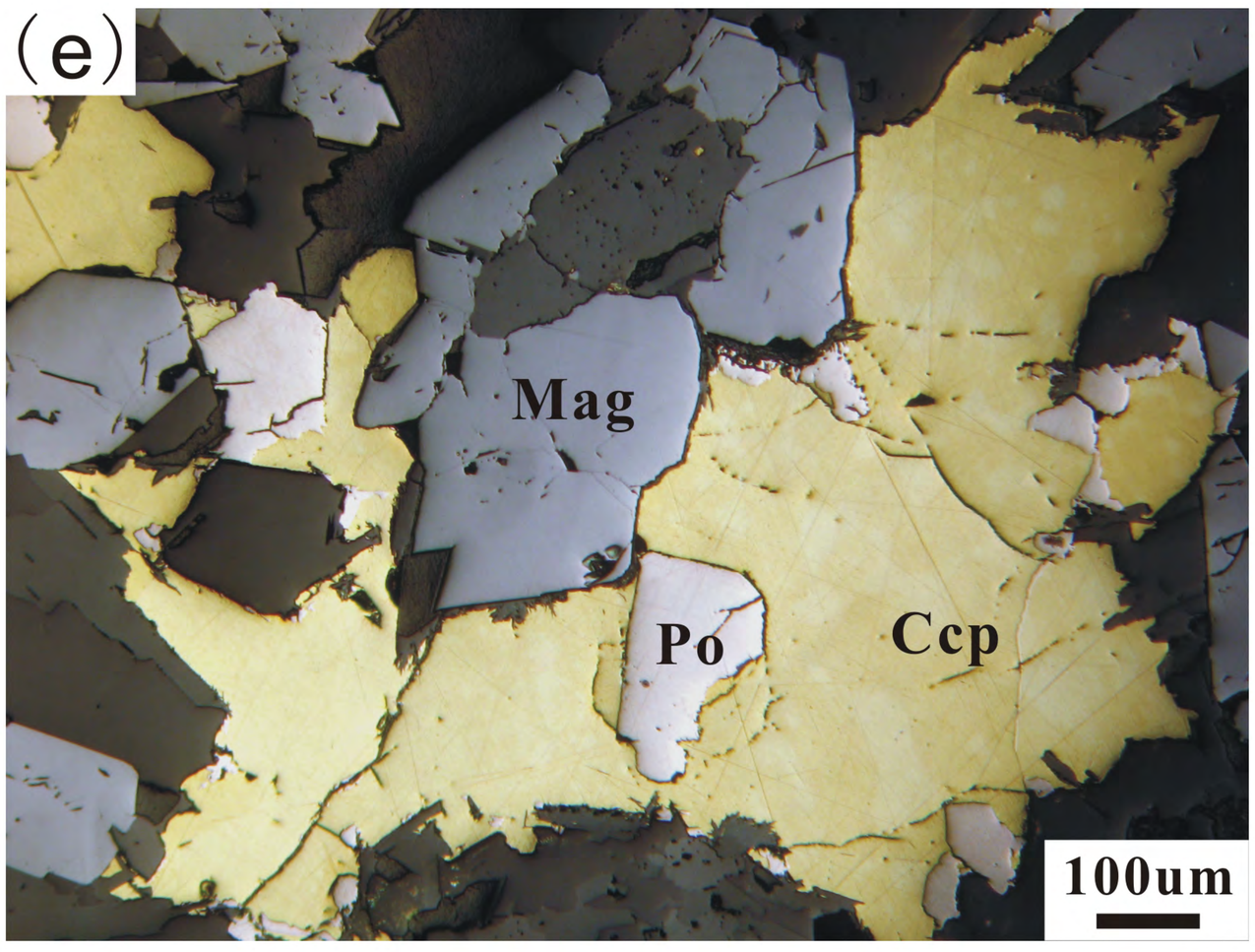
(e)
Mag
Po
Ccp
100um

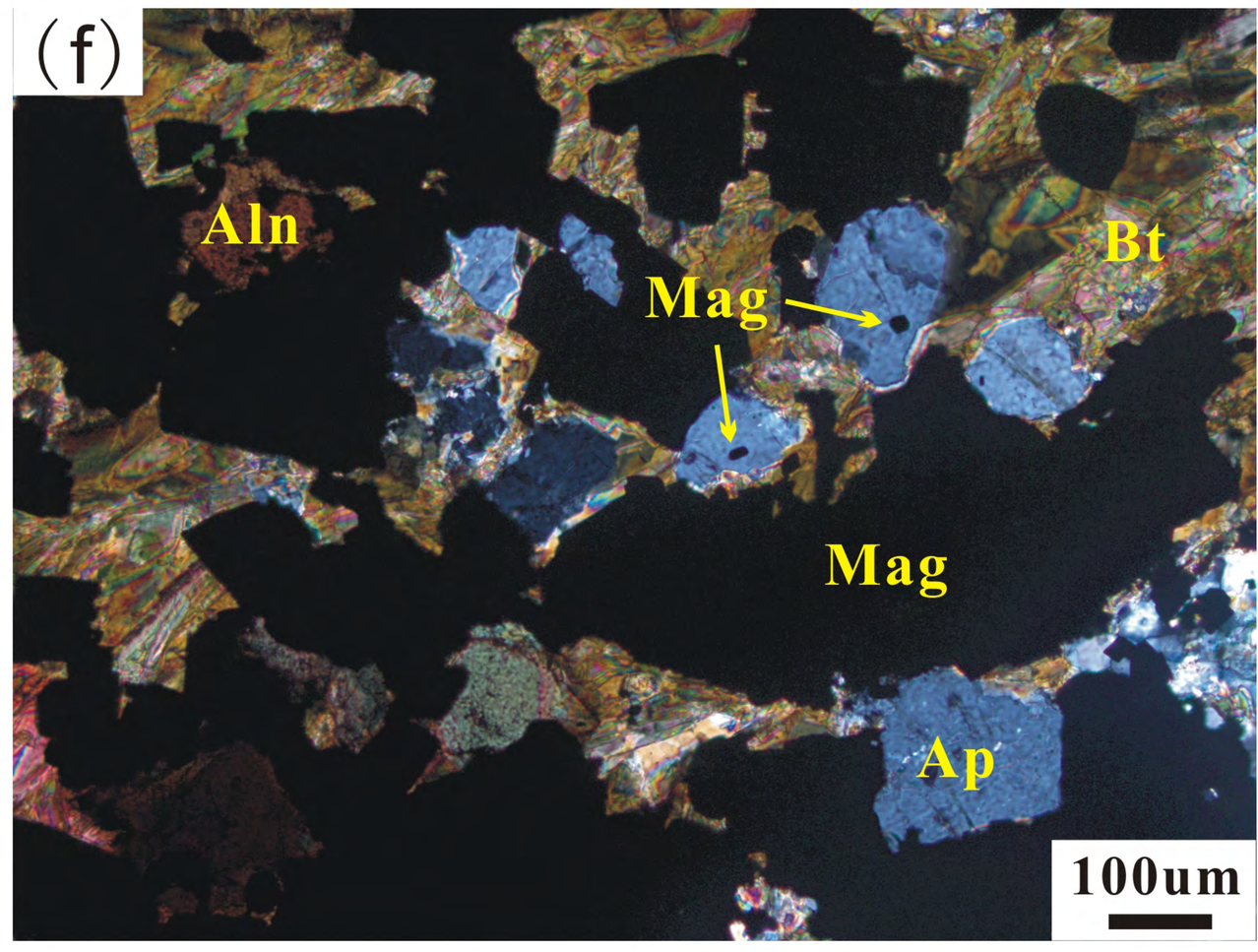
(f)
Aln
Bt
Mag
Mag
Ap
100um

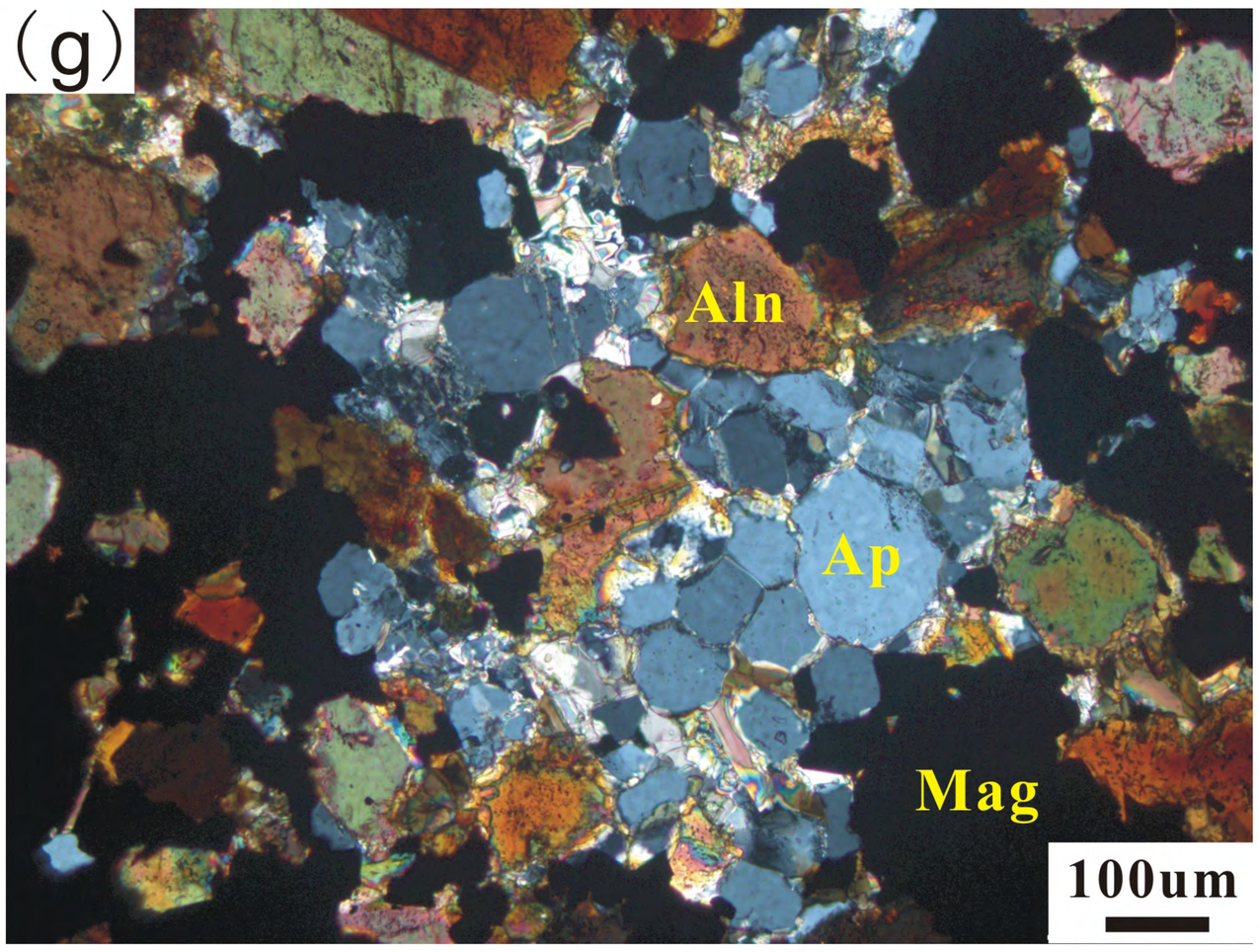
(g)
Aln
Ap
Mag
100um

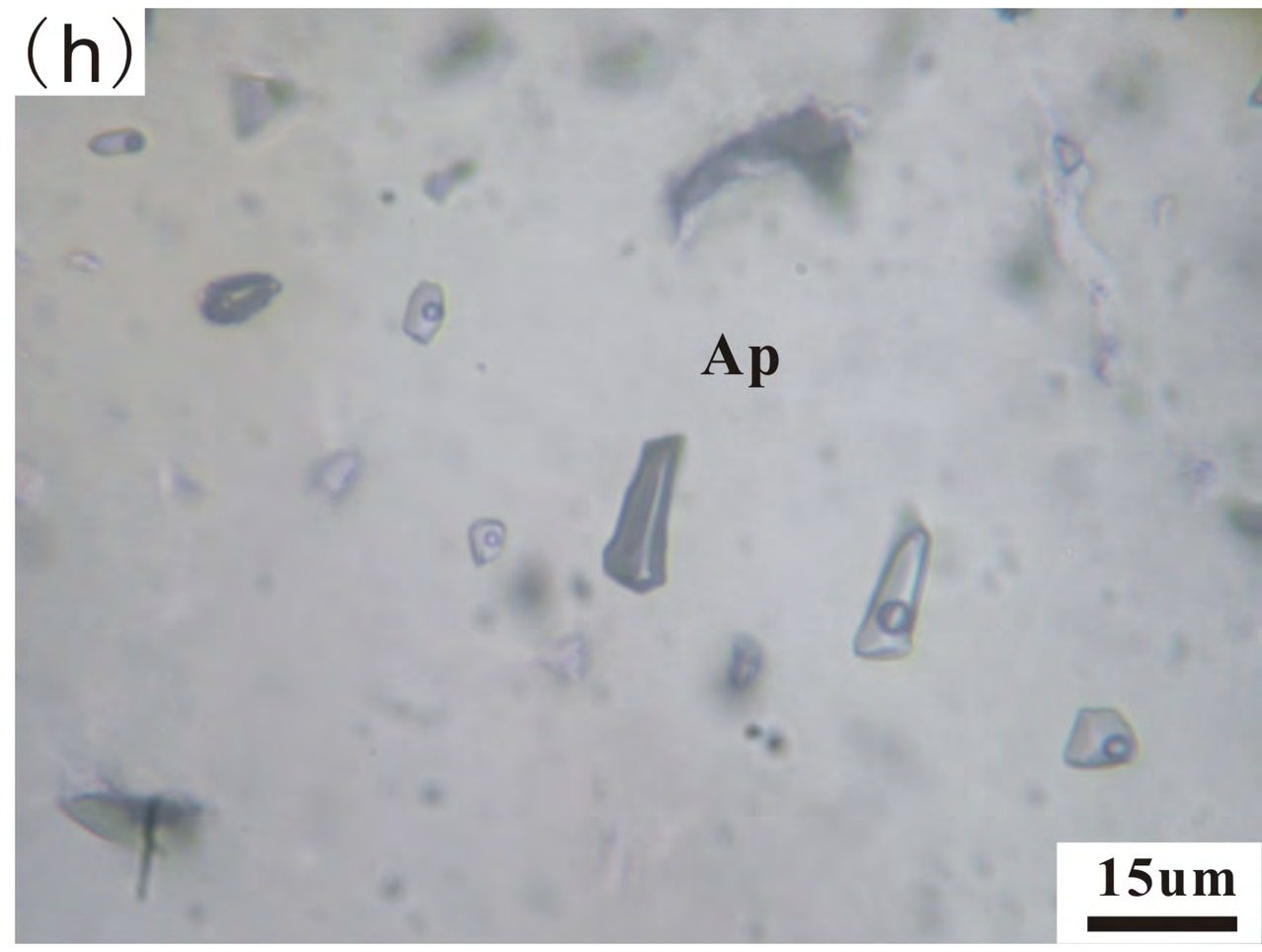
(h)
Ap
15um

Fig. 2

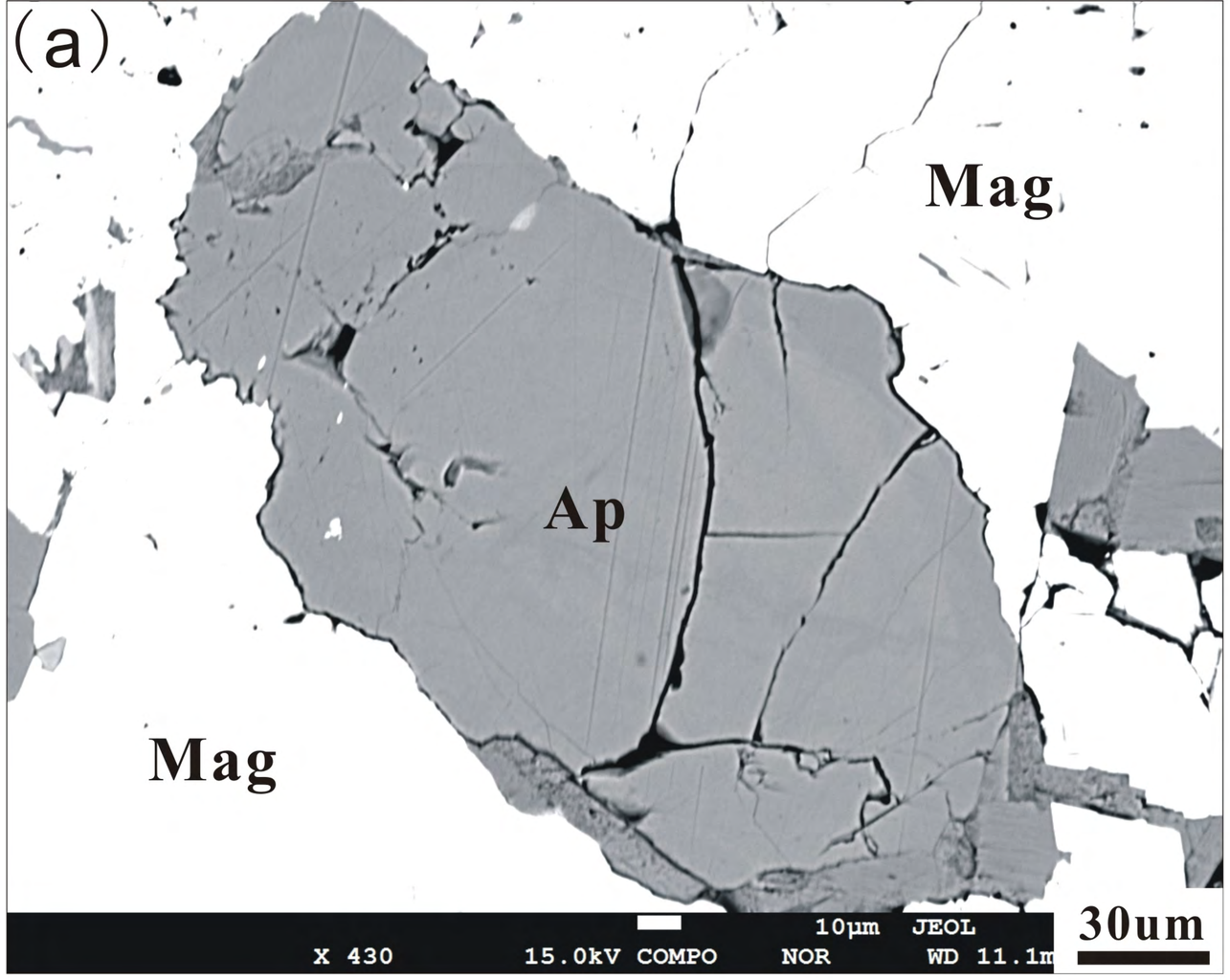
(a)
Mag
Ap
Mag
10μm JEOL
X 430 15.0kV COMPO NOR WD 11.1m
30um

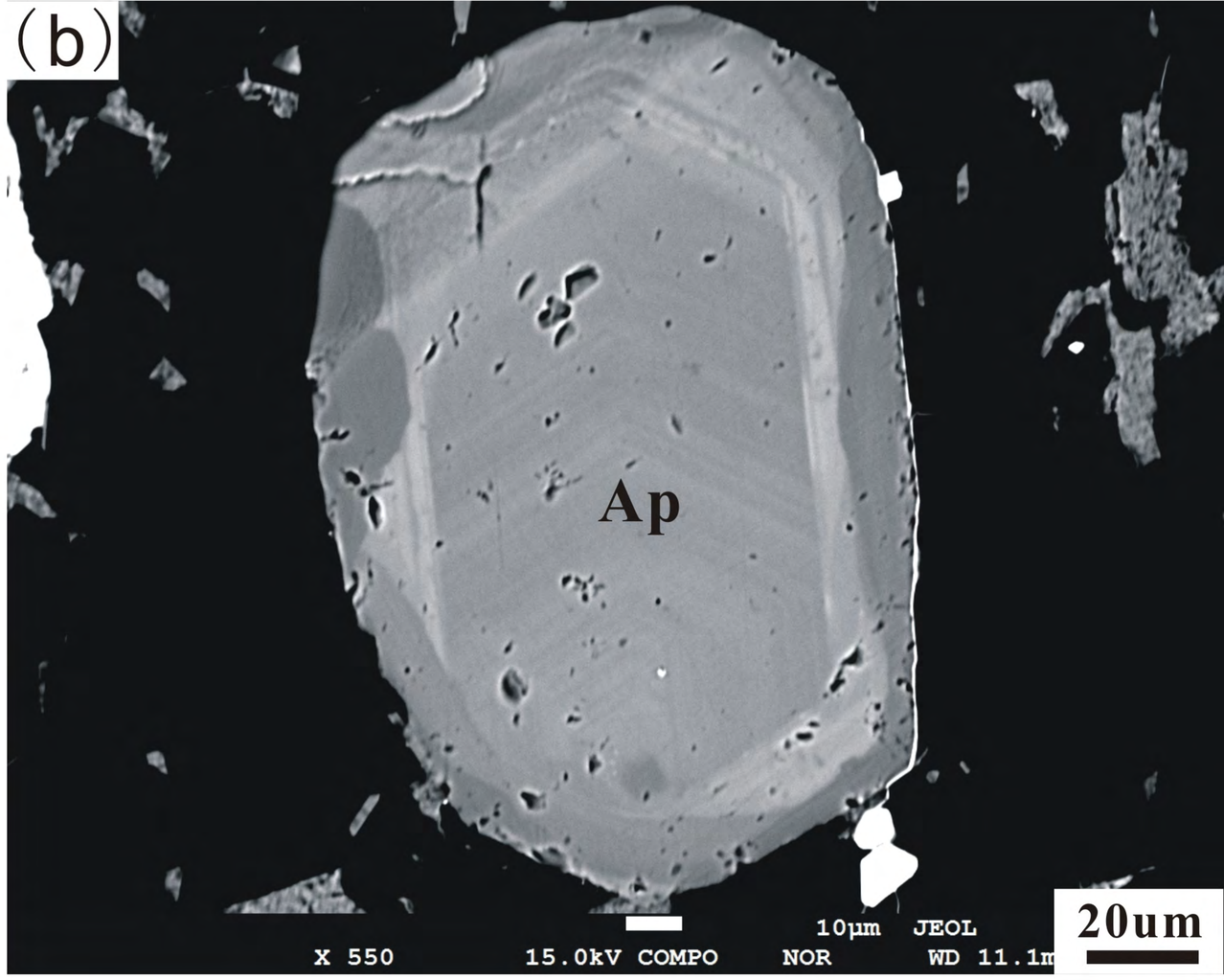
(b)
Ap
10μm JEOL
X 550 15.0kV COMPO NOR WD 11.1m
20um

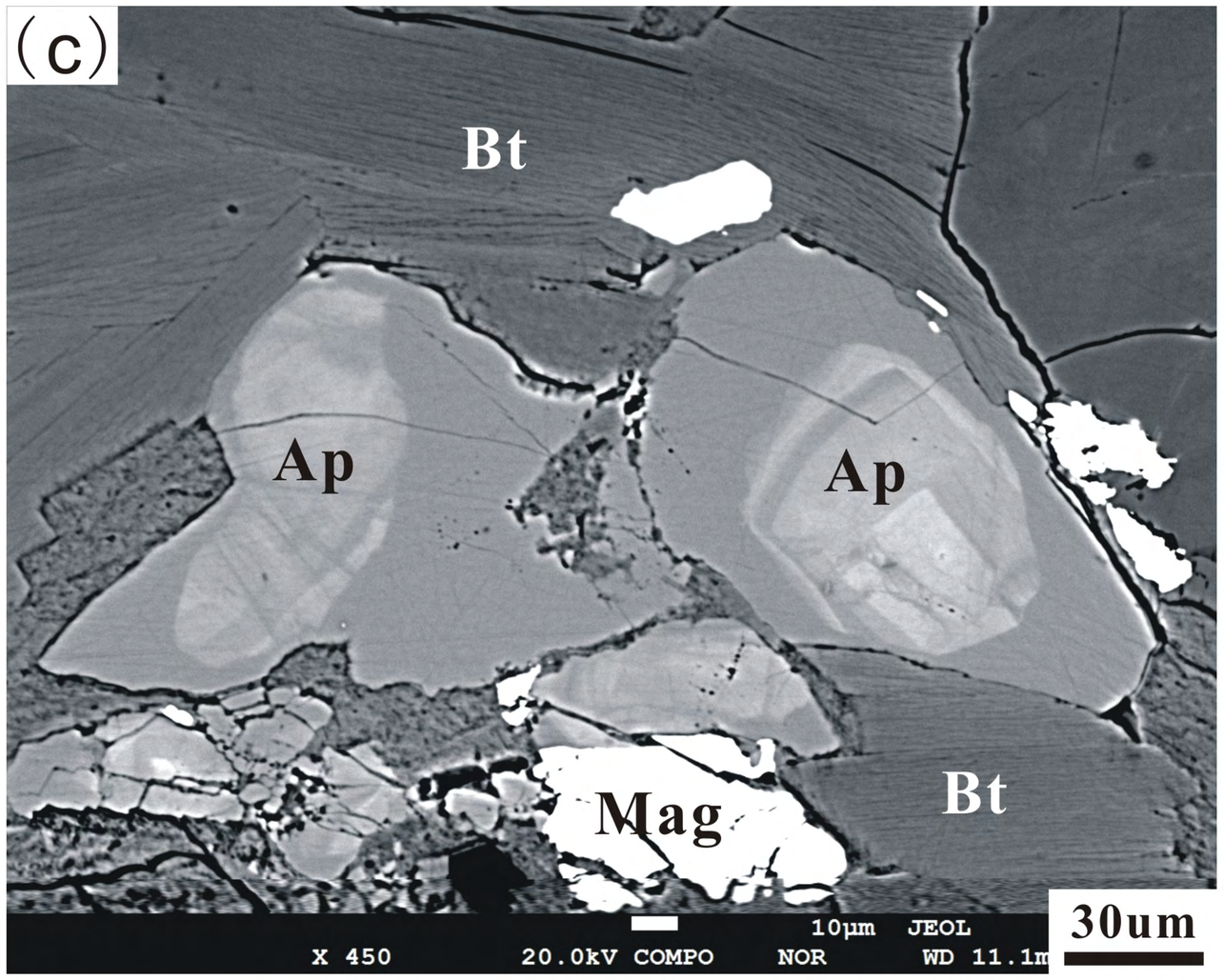
(c)
Bt
Ap
Ap
Mag
Bt
10μm JEOL
X 450 20.0kV COMPO NOR WD 11.1m
30um

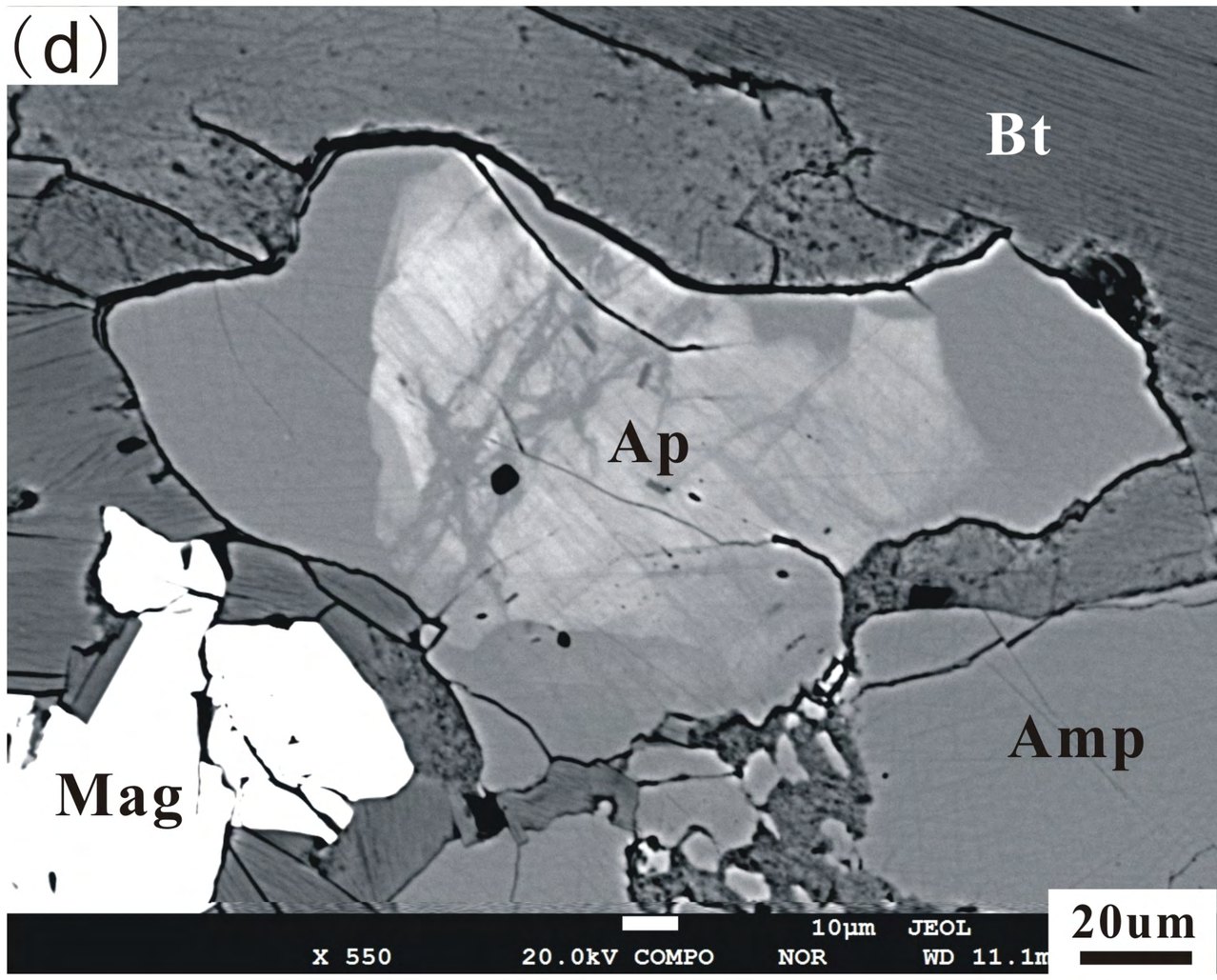
(d)
Bt
Ap
Amp
Mag
10μm JEOL
X 550 20.0kV COMPO NOR WD 11.1m
20um

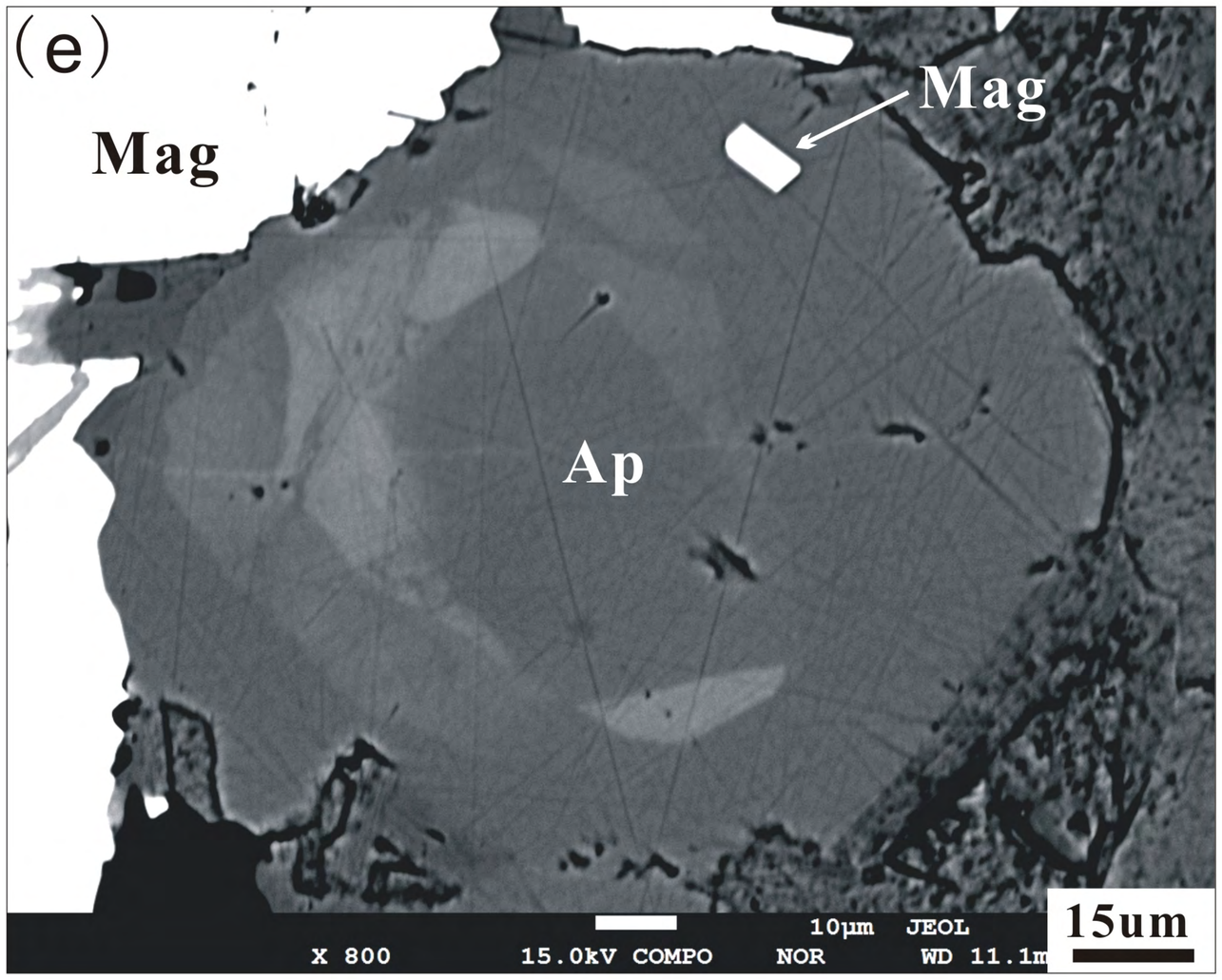
(e)
Mag
Mag
Ap
10μm JEOL
X 800 15.0kV COMPO NOR WD 11.1m
15um

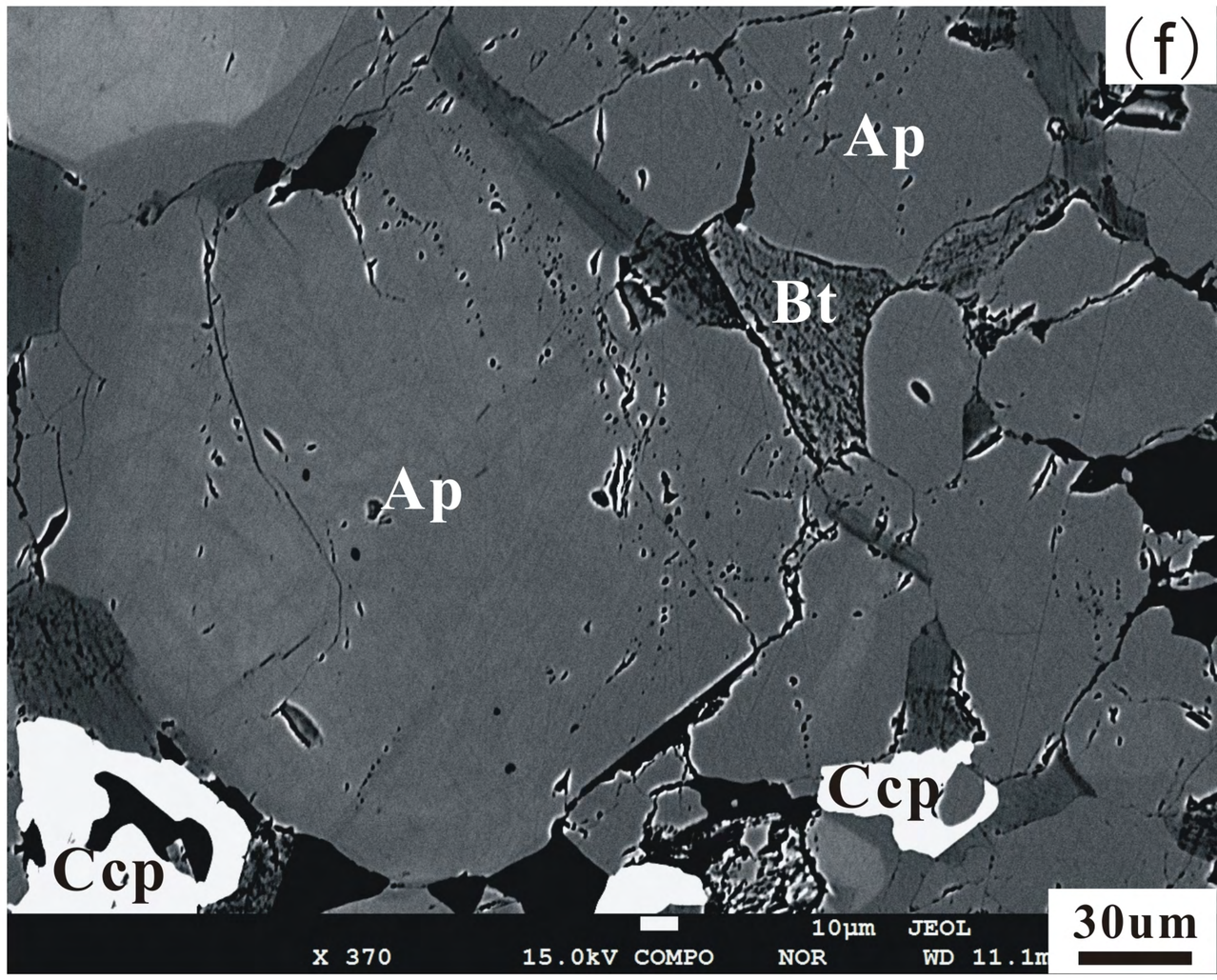
(f)
Ap
Bt
Ap
Ccp
Ccp
10μm JEOL
X 370 15.0kV COMPO NOR WD 11.1m
30um

Fig. 3

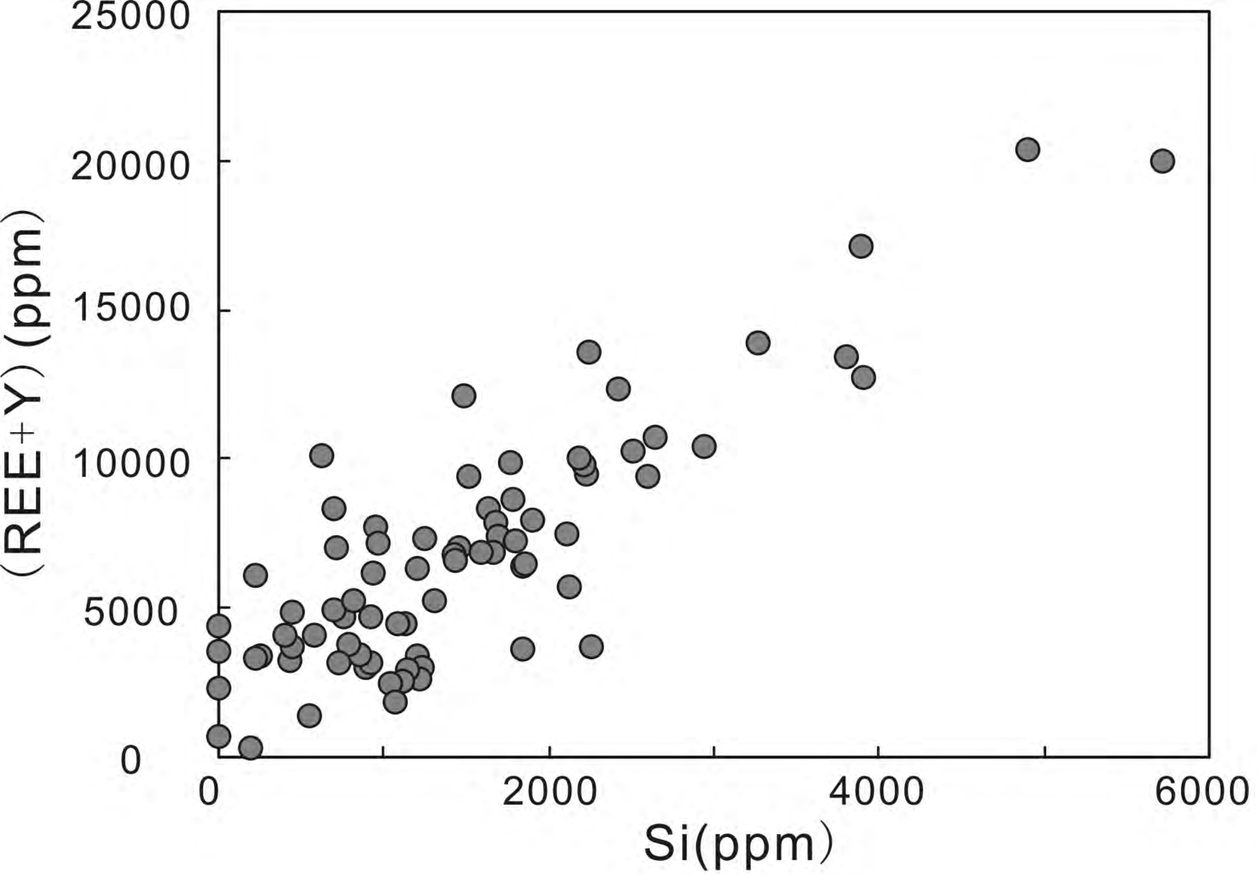
25000
20000
15000
10000
5000
0
(REE+Y) (ppm)
0
2000
4000
6000
Si(ppm)

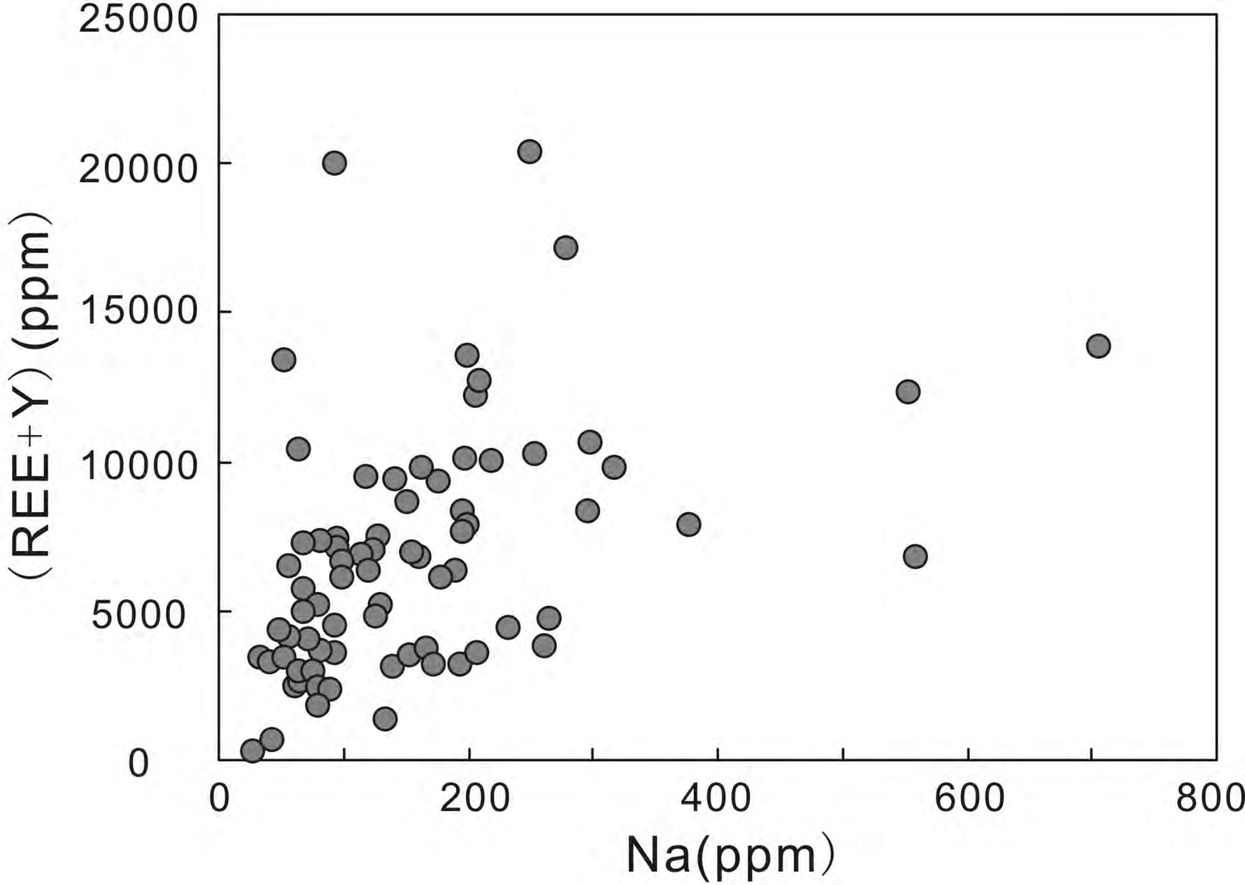
25000
20000
15000
10000
5000
0
(REE+Y) (ppm)
0
200
400
600
800
Na(ppm)

Fig. 4

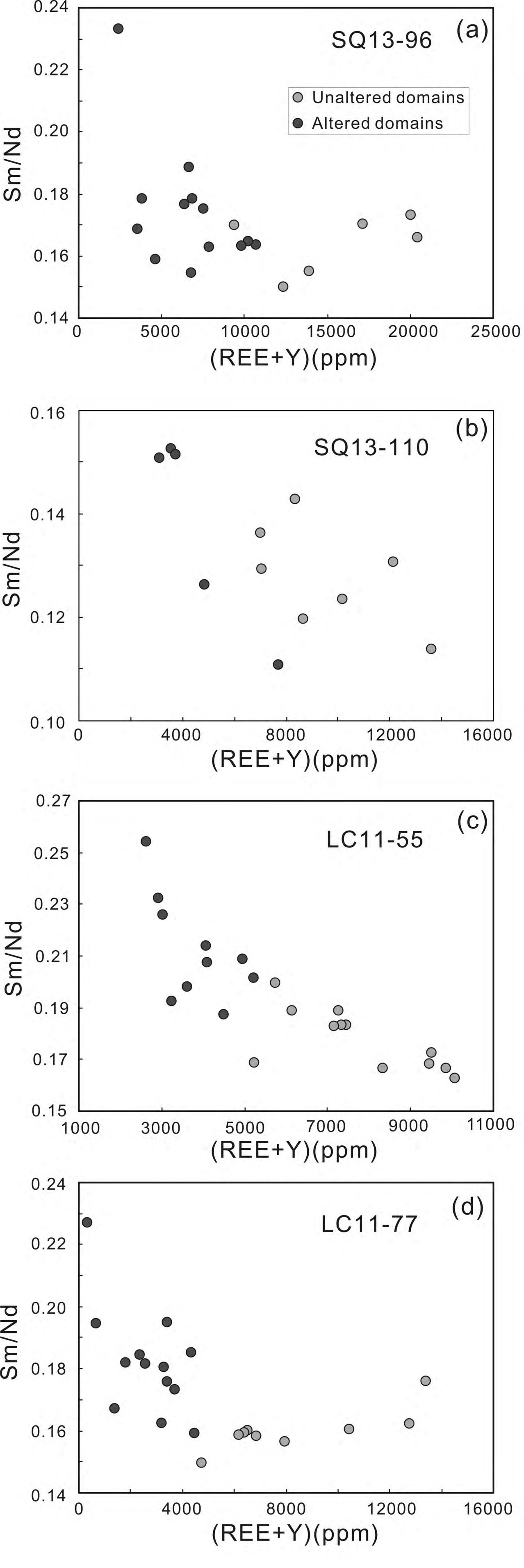
(a)
SQ13-96
Unaltered domains
Altered domains
Sm/Nd
(REE+Y)(ppm)
0.24
0.22
0.20
0.18
0.16
0.14
0
5000
10000
15000
20000
25000

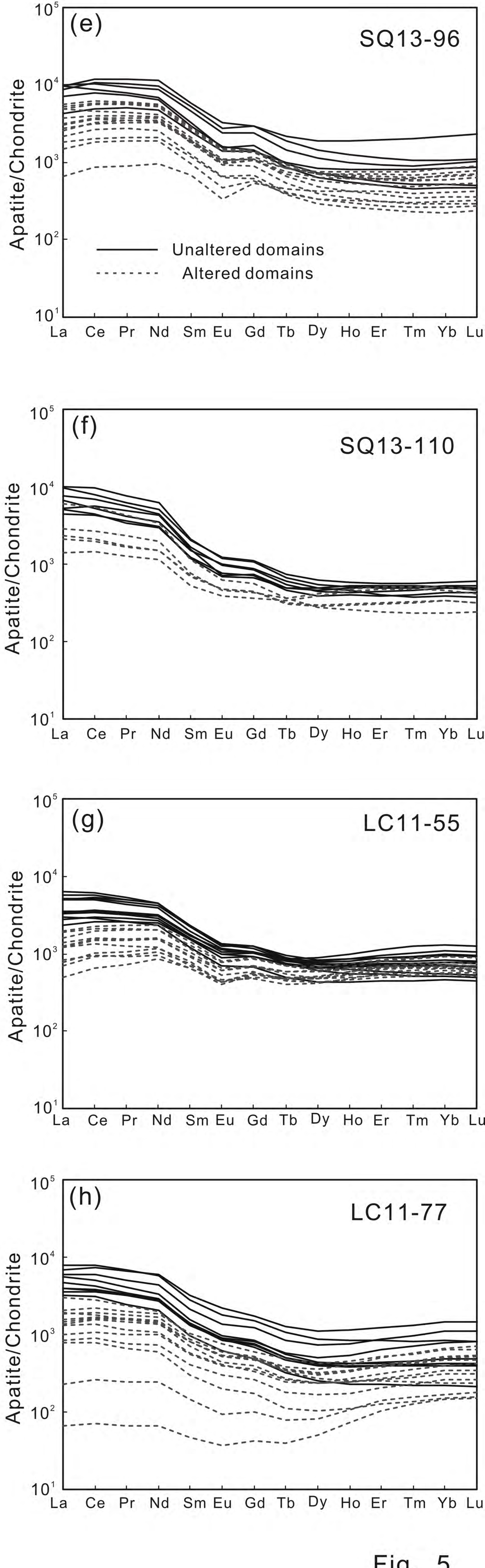
(e)
SQ13-96
Apatite/Chondrite
Unaltered domains
Altered domains
La
Ce
Pr
Nd
Sm
Eu
Gd
Tb
Dy
Ho
Er
Tm
Yb
Lu

(b)
SQ13-110
Sm/Nd
(REE+Y)(ppm)
0.16
0.14
0.12
0.10
0
4000
8000
12000
16000

(f)
SQ13-110
Apatite/Chondrite
La
Ce
Pr
Nd
Sm
Eu
Gd
Tb
Dy
Ho
Er
Tm
Yb
Lu

(c)
LC11-55
Sm/Nd
(REE+Y)(ppm)
0.27
0.25
0.23
0.21
0.19
0.17
0.15
1000
3000
5000
7000
9000
11000

(g)
LC11-55
Apatite/Chondrite
La
Ce
Pr
Nd
Sm
Eu
Gd
Tb
Dy
Ho
Er
Tm
Yb
Lu

(d)
LC11-77
Sm/Nd
(REE+Y)(ppm)
0.24
0.22
0.20
0.18
0.16
0.14
0
4000
8000
12000
16000

(h)
LC11-77
Apatite/Chondrite
La
Ce
Pr
Nd
Sm
Eu
Gd
Tb
Dy
Ho
Er
Tm
Yb
Lu

Fig. 5

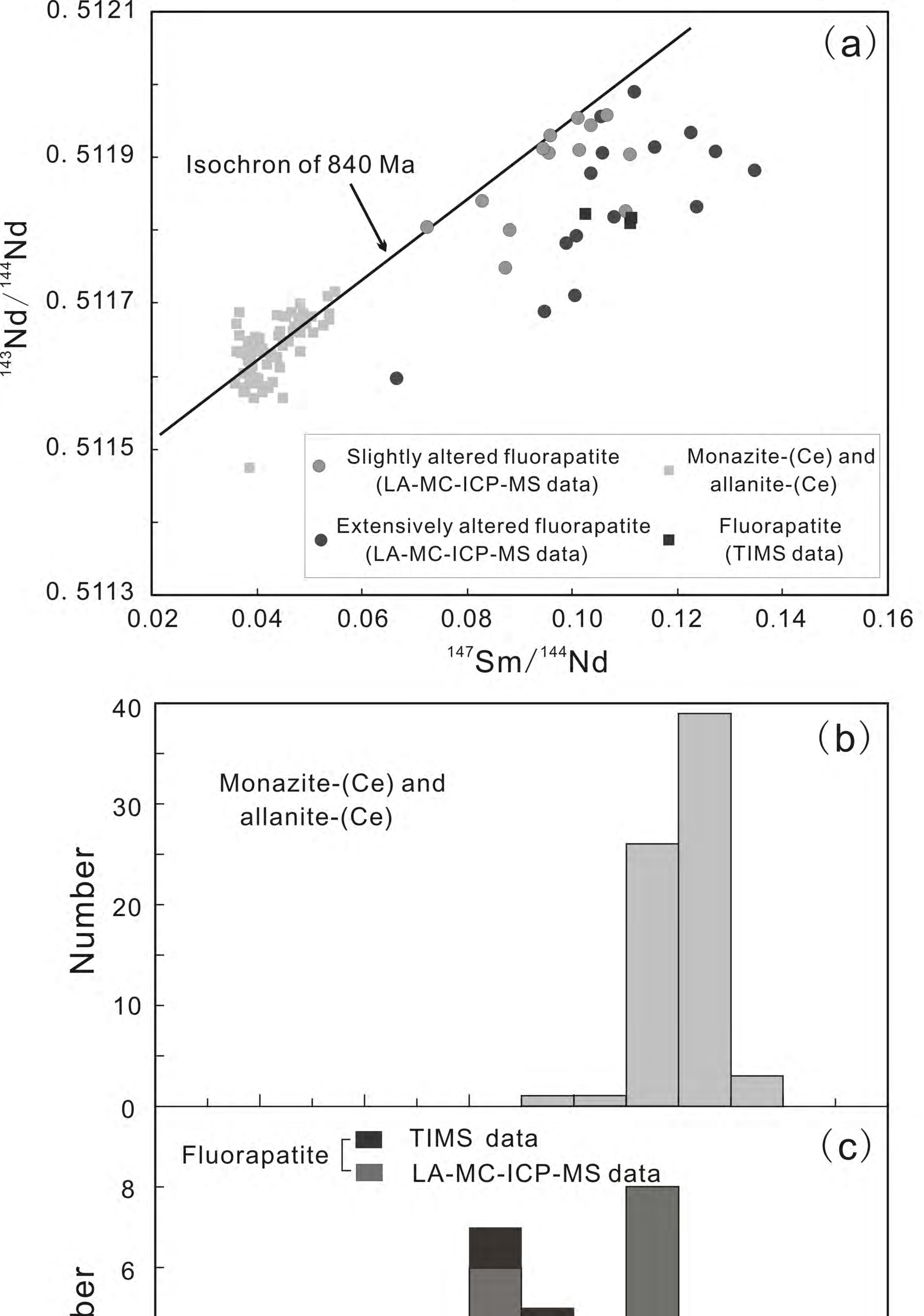
(a)
Isochron of 840 Ma
Slightly altered fluorapatite (LA-MC-ICP-MS data)
Monazite-(Ce) and allanite-(Ce)
Extensively altered fluorapatite (LA-MC-ICP-MS data)
Fluorapatite (TIMS data)
0. 5121
0. 5119
0. 5117
0. 5115
0. 5113
$^{143}Nd/^{144}Nd$
0.02
0.04
0.06
0.08
0.10
0.12
0.14
0.16
$^{147}Sm/^{144}Nd$
(b)
Monazite-(Ce) and allanite-(Ce)
Number
40
30
20
10
0
(c)
Fluorapatite
TIMS data
LA-MC-ICP-MS data
Number
8
6
4
2
0
0. 5110
0. 5112
0. 5114
0. 5116
$(^{143}Nd/^{144}Nd)_i$

Fig. 6

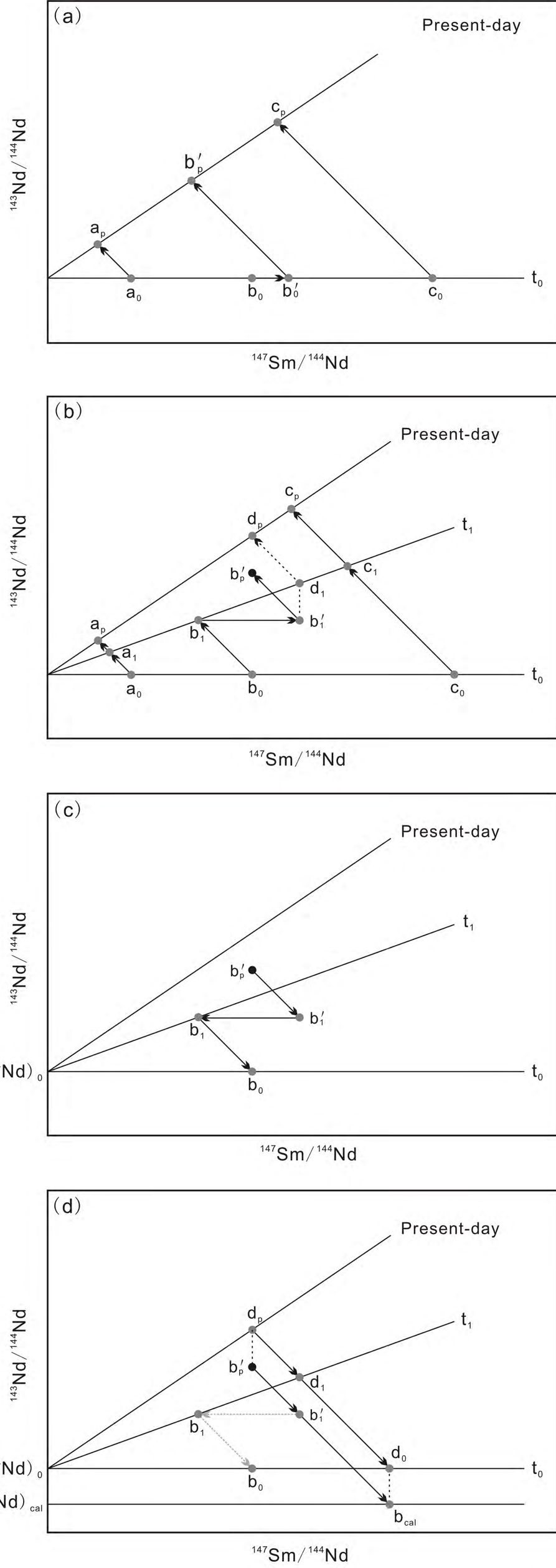
(a)
Present-day
$^{143}Nd/^{144}Nd$
$^{147}Sm/^{144}Nd$
c_p
b'_p
a_p
a_0
b_0
b'_0
c_0
t_0
(b)
Present-day
$^{143}Nd/^{144}Nd$
$^{147}Sm/^{144}Nd$
c_p
d_p
t_1
b'_p
c_1
d_1
b'_1
a_p
b_1
a_1
a_0
b_0
c_0
t_0
(c)
Present-day
$^{143}Nd/^{144}Nd$
$^{147}Sm/^{144}Nd$
t_1
b'_p
b'_1
b_1
$(^{143}Nd/^{144}Nd)_0$
b_0
t_0
(d)
Present-day
$^{143}Nd/^{144}Nd$
$^{147}Sm/^{144}Nd$
d_p
t_1
b'_p
d_1
b'_1
b_1
d_0
$(^{143}Nd/^{144}Nd)_0$
b_0
t_0
$(^{143}Nd/^{144}Nd)_{cal}$
b_{cal}

Fig. 7

Table 1 A list of fluorapatite-bearing samples

Sample No.	Locality	Rock type	Mineralogy
SQ13-96	North border of the western mining district	Massive ore sample	Stage I: Ab±Mag Stage II: Mag+Aln+Amp+Ap Stage III: Ccp+Bt±Py
SQ13-110	North border of the western mining district	Banded ore sample	Stage I: Ab+Chev+Mnz Stage II: Aln+Ap Stage III: Bt±Ccp
LC11-55	Ore pile in the eastern mining district	Banded ore sample	Stage II: Mag+Amp+Aln+Bt+Ap Stage III: Ccp
LC11-77	Ore pile in the eastern mining district	Massive ore sample	Stage II: Mag+Aln+Bt+Amp+Ap Stage III: Ccp+Po

Table 2 A summary of major element content of fluorapatite (wt.%)

	BSE-bright domains		BSE-dark domains	
	Mean (n=58)	Range	Mean (n=58)	Range
SO_3	0.01	b.d.l.-0.05	0.01	b.d.l.-0.04
P_2O_5	41.64	40.42-42.48	42.26	41.48-42.99
SiO_2	0.31	b.d.l.-1.01	b.d.l.	b.d.l.-0.08
Ce_2O_3	0.57	b.d.l.-1.29	0.16	b.d.l.-0.57
FeO	0.19	0.01-0.57	0.20	0.01-0.64
MnO	0.02	b.d.l.-0.08	0.02	b.d.l.-0.07
CaO	54.66	53.19-55.59	55.12	54.51-55.76
SrO	0.07	b.d.l.-0.14	0.09	0.02-0.22
Na_2O	b.d.l.	b.d.l.-0.04	b.d.l.	b.d.l.-0.05
F	2.80	2.39-3.71	2.87	2.44-3.67
Cl	0.01	b.d.l.-0.02	0.01	b.d.l.-0.02
OH	0.83	0.01-1.23	0.80	0.08-1.19
Total	99.93	98.51-100.82	100.33	99.01-100.89

Note: (1) b.d.l. means below detection limit. (2) The content of OH was estimated assuming the (F, Cl, OH) site is filled.

Table 3 A summary of trace element concentration for fluorapatite (ppm)

	SQ13-96 (BSE-bright domains)		SQ13-96 (BSE-dark domains)		SQ13-110 (BSE-bright domains)		SQ13-110 (BSE-dark domains)	
	Mean (n=6)	Range	Mean (n=13)	Range	Mean (n=7)	Range	Mean (n=5)	Range
Na	343	93.6-706	244	79.8-558	190	124-295	155	125-196
Si	3802	2426-5720	1617	784-2646	1286	618-2247	876	b.d.l.-2263
Sc	0.35	0.04-0.81	0.20	0.11-0.40	0.28	0.15-0.40	0.28	0.22-0.38
V	1.17	0.15-4.61	0.30	0.05-0.71	0.15	0.11-0.23	0.16	b.d.l.-0.32
Cr	1.60	0.79-3.34	0.92	b.d.l.-1.97	2.02	b.d.l.-3.53	2.25	b.d.l.-5.53
Ge	27.9	15.8-40.9	12.0	3.02-19.9	31.4	11.3-50.8	13.6	5.44-28.4
As	141	43.8-281	63.7	14.4-158	45.1	8.67-96.0	42.4	5.06-81.5
Rb	0.45	0.09-1.75	0.22	0.03-1.05	0.12	0.02-0.17	0.12	0.08-0.15
Sr	596	457-780	619	442-735	746	474-873	811	788-836
Ba	0.71	0.06-1.65	0.44	0.03-3.33	0.50	0.11-1.73	1.18	0.46-2.07
Pb	2.32	1.86-2.62	2.00	1.72-2.30	2.11	1.43-2.86	1.92	1.74-2.16
Th	9.69	2.95-18.1	2.01	0.36-4.28	5.71	1.94-12.8	2.11	1.03-3.41
U	109	44.6-204	29.4	9.46-57.0	51.4	30.1-110	24.8	19.7-31.7
La	1933	1021-2346	760	156-1328	1651	1053-2359	700	337-1430
Ce	5472	2989-7156	2221	521-3787	3822	2601-5829	1673	894-3338
Pr	816	472-1128	344	84.7-568	485	325-736	214	121-413
Nd	3711	2226-5303	1626	450-2607	1957	1361-2869	889	534-1601
Sm	612	379-880	276	105-427	247	184-327	117	80.4-177
Eu	125	78.9-190	55.1	19.4-84.7	54.0	40.6-71.2	28.0	22.6-36.2
Gd	435	281-605	204	108-292	176	138-228	91.9	73.5-116
Tb	51.3	32.3-79.5	24.8	14.2-35.2	21.5	17.1-28.0	12.5	11.6-13.3
Dy	281	163-477	138	73.7-189	125	97.8-156	84.4	70.4-105
Ho	57.2	31.0-104	28.7	14.8-41.9	27.3	22.6-32.6	20.1	14.6-26.7
Er	161	82.5-319	81.0	39.9-125	78.8	64.8-92.6	61.6	39.3-85.4
Tm	24.0	11.5-50.5	12.0	5.87-19.4	12.1	9.50-14.3	9.59	6.00-13.2
Yb	170	78.5-369	83.8	37.6-139	83.3	65.1-100	64.0	39.5-87.6
Lu	26.3	11.8-58.2	13.1	6.02-22.2	12.2	9.65-15.3	8.89	6.08-11.8
Y	1643	933-3002	858	445-1280	804	724-963	619	402-816
Total (REE+Y)	15517	9379-20388	6725	2439-10688	9556	6999-13596	4594	3138-7704
Sm/Nd	0.164	0.150-0.173	0.174	0.154-0.233	0.128	0.114-0.143	0.138	0.111-0.153

	LC11-55 (BSE-bright domains)		LC11-55 (BSE-dark domains)		LC11-77 (BSE-bright domains)		LC11-77 (BSE-dark domains)	
	Mean (n=12)	Range	Mean (n=11)	Range	Mean (n=9)	Range	Mean (n=13)	Range
Na	123	67.8-218	83.6	55.9-192.3	145	51.4-266	84.0	27.2-232
Si	1516	222-2233	990	396-1835	2108	753-3905	544	b.d.l.-1203
Sc	0.32	0.26-0.42	0.24	0.10-0.38	0.44	0.16-0.81	0.35	0.15-0.57
V	0.50	0.26-1.03	0.38	0.16-0.89	1.09	0.26-1.97	0.38	b.d.l.-0.73
Cr	2.83	0.83-4.39	2.81	1.37-4.26	1.81	0.29-3.69	2.88	0.91-4.53
Ge	21.2	13.5-28.6	9.01	4.89-14.9	21.1	10.4-41.2	7.72	1.11-14.2
As	84.6	38.3-244	49.5	18.2-93.7	88.5	7.81-195	49.5	14.2-89.9
Rb	0.33	0.12-1.23	0.29	0.10-0.74	0.85	0.07-2.20	0.35	0.02-0.98
Sr	555	388-688	702	588-822	899	712-1137	1039	736-1645
Ba	0.55	0.12-1.90	0.64	0.16-2.64	1.59	0.09-4.36	0.54	0.07-2.62
Pb	1.75	1.07-2.13	2.02	1.80-2.44	1.98	1.27-2.54	2.15	1.31-2.72
Th	2.35	0.83-3.41	0.77	0.44-1.24	2.70	0.47-6.95	0.35	b.d.l.-0.88
U	50.5	29.8-63.1	26.9	17.8-45.6	60.8	12.4-171	14.8	0.78-33.7
La	963	545-1511	286	117-469	1207	774-1847	318	15.6-715
Ce	2530	1578-3773	876	403-1393	3047	1899-4750	851	42.9-1708
Pr	360	247-501	137	68.5-220	403	236-641	119	6.28-224
Nd	1610	1094-2119	691	396-1091	1699	970-2785	537	31.4-926
Sm	283	184-357	145	99.0-220	275	145-490	95.0	7.13-158
Eu	63.7	40.7-76.5	32.1	23.1-46.1	67.0	35.3-126	24.1	2.12-44.5
Gd	216	139-258	131	98.5-183	201	100-359	74.6	8.70-125
Tb	29.9	18.6-35.0	19.9	15.2-25.9	25.4	12.0-47.9	9.91	1.50-17.9
Dy	180	108-222	133	106-170	145	63.8-281	60.6	12.8-107
Ho	40.7	24.0-55.6	32.7	25.7-41.6	32.4	13.0-64.5	14.6	4.10-25.5
Er	125	72.7-185	107	82.9-137	100	37.9-204	49.4	17.2-85.8
Tm	19.8	11.5-31.7	17.3	13.2-22.3	16.2	5.53-33.3	8.38	3.25-14.7
Yb	136	78.0-221	119	91.9-155	117	37.6-252	62.7	24.5-114
Lu	19.6	11.2-31.6	17.1	13.1-22.4	17.3	5.40-37.3	9.63	3.80-18.0
Y	1205	742-1645	1012	807-1246	991	390-1902	460	138-785
Total (REE+Y)	7782	5224-10053	3757	2638-5218	8344	4727-13400	2693	319-4467
Sm/Nd	0.178	0.163-0.200	0.213	0.187-0.254	0.160	0.150-0.176	0.182	0.159-0.227

Table 4 In-situ Sm-Nd isotopic data for fluorapatite, monazite-(Ce) and allanite-(Ce)

	Intensity of ^{142}Nd (V)	$^{147}Sm/^{144}Nd$	2σ	$^{143}Nd/^{144}Nd$	2σ	$^{145}Nd/^{144}Nd$	2σ	$(^{143}Nd/^{144}Nd)_i$	εNd(t=840Ma)	Mark
Fluorapatite										
SQ13-96-1	1.6	0.1066	0.0002	0.51196	0.00005	0.34836	0.00003	0.51137	-3.6	Dominated by BSE-bright area
SQ13-96-2	0.7	0.1005	0.0002	0.51171	0.00009	0.34840	0.00006	0.51116	-7.8	Dominated by BSE-dark area
SQ13-96-3	1.1	0.0882	0.0005	0.51180	0.00008	0.34838	0.00004	0.51131	-4.7	Higher proportion of BSE-bright area
SQ13-96-4	1.1	0.1157	0.0002	0.51191	0.00006	0.34839	0.00004	0.51128	-5.4	Higher proportion of BSE-dark area
SQ13-96-5	1.9	0.0957	0.0001	0.51193	0.00005	0.34839	0.00003	0.51140	-2.9	Dominated by BSE-bright area
SQ13-96-6	2.5	0.0945	0.0001	0.51191	0.00004	0.34839	0.00003	0.51139	-3.2	Dominated by BSE-bright area
SQ13-96-7	1.0	0.1007	0.0001	0.51179	0.00006	0.34842	0.00004	0.51124	-6.2	Higher proportion of BSE-dark area
SQ13-96-8	0.9	0.0988	0.0001	0.51178	0.00007	0.34836	0.00005	0.51124	-6.2	Dominated by BSE-dark area
SQ13-96-9	0.7	0.1079	0.0002	0.51182	0.00009	0.34834	0.00006	0.51122	-6.5	Dominated by BSE-dark area
SQ13-96-10	0.7	0.0872	0.0002	0.51175	0.00009	0.34836	0.00006	0.51127	-5.6	Higher proportion of BSE-bright area
SQ13-110-1	1.0	0.1226	0.0002	0.51194	0.00007	0.34833	0.00004	0.51126	-5.8	Dominated by BSE-dark area
SQ13-110-2	1.5	0.1057	0.0002	0.51191	0.00005	0.34841	0.00004	0.51132	-4.5	Higher proportion of BSE-dark area
SQ13-110-3	1.8	0.0828	0.0009	0.51184	0.00005	0.34838	0.00003	0.51139	-3.3	Dominated by BSE-bright area
SQ13-110-4	2.6	0.0723	0.0002	0.51180	0.00004	0.34838	0.00003	0.51141	-2.9	Dominated by BSE-bright area
SQ13-110-5	1.0	0.0667	0.0002	0.51160	0.00008	0.34835	0.00005	0.51123	-6.3	Higher proportion of BSE-dark area
LC11-55-1	1.0	0.1272	0.0002	0.51191	0.00006	0.34841	0.00004	0.51121	-6.8	Higher proportion of BSE-dark area
LC11-55-2	0.7	0.1237	0.0002	0.51183	0.00008	0.34833	0.00005	0.51115	-7.9	Higher proportion of BSE-dark area
LC11-55-3	0.8	0.1348	0.0002	0.51188	0.00007	0.34838	0.00005	0.51114	-8.1	Dominated by BSE-dark area
LC11-55-4	1.1	0.1012	0.0002	0.51191	0.00007	0.34839	0.00004	0.51135	-3.9	Dominated by BSE-bright area
LC11-55-5	1.1	0.1102	0.0002	0.51183	0.00006	0.34841	0.00004	0.51122	-6.5	Dominated by BSE-bright area
LC11-55-6	1.0	0.1110	0.0002	0.51190	0.00007	0.34835	0.00004	0.51129	-5.1	Higher proportion of BSE-bright area

LC11-77-1	0.6	0.0948	0.0003	0.51169	0.00009	0.34840	0.00007	0.51117	-7.6	Dominated by BSE-dark area
LC11-77-2	1.8	0.0955	0.0001	0.51191	0.00005	0.34837	0.00003	0.51138	-3.4	Dominated by BSE-bright area
LC11-77-3	1.3	0.1055	0.0001	0.51196	0.00005	0.34836	0.00003	0.51138	-3.5	Higher proportion of BSE-dark area
LC11-77-4	1.5	0.1011	0.0001	0.51195	0.00005	0.34839	0.00004	0.51140	-3.1	Dominated by BSE-bright area
LC11-77-5	1.6	0.1034	0.0001	0.51195	0.00004	0.34840	0.00003	0.51138	-3.5	Dominated by BSE-bright area
LC11-77-6	1.4	0.1117	0.0001	0.51199	0.00005	0.34837	0.00003	0.51138	-3.5	Dominated by BSE-dark area
LC11-77-7	1.0	0.1034	0.0001	0.51188	0.00005	0.34841	0.00004	0.51131	-4.8	Dominated by BSE-dark area
Monazite-(Ce)										
LC11-44-1	5.4	0.0505	0.0003	0.51168	0.00003	0.34845	0.00002	0.51140	-3.0	
LC11-44-2	5.5	0.0494	0.0001	0.51167	0.00003	0.34841	0.00002	0.51140	-3.0	
LC11-44-3	5.8	0.0549	0.0003	0.51172	0.00003	0.34842	0.00002	0.51141	-2.8	
LC11-44-4	5.3	0.0483	0.0002	0.51166	0.00003	0.34843	0.00002	0.51139	-3.2	
LC11-44-5	5.5	0.0537	0.0001	0.51171	0.00004	0.34842	0.00002	0.51141	-2.8	
LC11-44-6	4.8	0.0539	0.0002	0.51168	0.00004	0.34842	0.00003	0.51138	-3.4	
LC11-44-7	5.1	0.0539	0.0001	0.51169	0.00004	0.34843	0.00002	0.51139	-3.2	
LC11-44-8	5.3	0.0481	0.0002	0.51168	0.00005	0.34842	0.00004	0.51141	-2.7	
LC11-44-9	5.0	0.0484	0.0002	0.51163	0.00005	0.34841	0.00004	0.51137	-3.7	
LC11-44-10	5.4	0.0444	0.0001	0.51166	0.00004	0.34844	0.00003	0.51142	-2.7	
LC11-44-11	4.3	0.0527	0.0002	0.51167	0.00005	0.34844	0.00003	0.51138	-3.4	
LC11-44-12	4.0	0.0490	0.0001	0.51168	0.00005	0.34845	0.00004	0.51141	-2.9	
SQ13-99-1	5.1	0.0440	0.0000	0.51168	0.00003	0.34845	0.00002	0.51144	-2.2	
SQ13-99-2	4.6	0.0375	0.0000	0.51160	0.00003	0.34840	0.00002	0.51140	-3.1	
SQ13-99-3	4.6	0.0419	0.0000	0.51161	0.00003	0.34841	0.00002	0.51138	-3.3	
SQ13-99-4	4.8	0.0414	0.0000	0.51159	0.00003	0.34841	0.00002	0.51136	-3.8	
SQ13-99-5	4.8	0.0411	0.0000	0.51158	0.00003	0.34840	0.00002	0.51135	-4.0	
SQ13-99-6	4.3	0.0424	0.0000	0.51158	0.00003	0.34842	0.00002	0.51135	-4.0	

SQ13-99-7	4.2	0.0415	0.0001	0.51163	0.00004	0.34844	0.00002	0.51140	-3.0
SQ13-99-8	4.1	0.0449	0.0000	0.51157	0.00004	0.34840	0.00002	0.51132	-4.6
SQ13-99-9	4.4	0.0429	0.0000	0.51163	0.00003	0.34840	0.00002	0.51139	-3.2
SQ13-99-10	4.1	0.0470	0.0000	0.51166	0.00004	0.34841	0.00003	0.51140	-3.0
SQ13-99-11	3.9	0.0391	0.0000	0.51161	0.00005	0.34845	0.00004	0.51140	-3.1
Allanite-(Ce)									
LC11-77-1	4.9	0.0405	0.0001	0.51160	0.00003	0.34838	0.00002	0.51137	-3.6
LC11-77-2	5.0	0.0379	0.0000	0.51158	0.00003	0.34841	0.00002	0.51138	-3.5
LC11-77-3	5.2	0.0388	0.0000	0.51159	0.00003	0.34841	0.00002	0.51137	-3.5
LC11-77-4	6.3	0.0412	0.0002	0.51164	0.00003	0.34841	0.00002	0.51141	-2.8
LC11-77-5	6.1	0.0395	0.0000	0.51159	0.00003	0.34841	0.00002	0.51137	-3.6
LC11-77-6	6.1	0.0388	0.0000	0.51163	0.00003	0.34842	0.00002	0.51141	-2.8
LC11-77-7	5.7	0.0392	0.0000	0.51161	0.00003	0.34840	0.00002	0.51140	-3.1
LC11-77-8	5.7	0.0398	0.0001	0.51160	0.00003	0.34841	0.00002	0.51138	-3.4
LC11-77-9	4.7	0.0391	0.0000	0.51160	0.00003	0.34840	0.00002	0.51139	-3.3
LC11-56-1	6.6	0.0395	0.0000	0.51163	0.00003	0.34841	0.00002	0.51142	-2.7
LC11-56-2	6.8	0.0387	0.0000	0.51163	0.00004	0.34841	0.00003	0.51142	-2.6
LC11-56-3	2.7	0.0396	0.0001	0.51157	0.00006	0.34838	0.00004	0.51135	-4.0
LC11-56-4	2.4	0.0389	0.0001	0.51147	0.00007	0.34841	0.00005	0.51126	-5.8
LC11-56-5	6.8	0.0386	0.0000	0.51162	0.00003	0.34841	0.00002	0.51141	-2.8
LC11-56-6	6.8	0.0385	0.0000	0.51165	0.00003	0.34841	0.00002	0.51144	-2.3
LC11-56-7	6.7	0.0388	0.0000	0.51162	0.00003	0.34840	0.00002	0.51140	-2.9
LC11-56-8	6.0	0.0390	0.0000	0.51162	0.00003	0.34843	0.00002	0.51141	-2.9
LC11-56-9	25.6	0.0399	0.0000	0.51165	0.00003	0.34841	0.00002	0.51143	-2.4
LC11-56-10	25.4	0.0397	0.0000	0.51164	0.00001	0.34841	0.00001	0.51142	-2.6
SQ13-99-1	2.5	0.0359	0.0001	0.51159	0.00005	0.34836	0.00003	0.51139	-3.2

SQ13-110-1	3.9	0.0462	0.0001	0.51165	0.00004	0.34840	0.00003	0.51139	-3.2
SQ13-110-2	5.8	0.0508	0.0000	0.51166	0.00003	0.34840	0.00002	0.51138	-3.4
SQ13-110-3	6.0	0.0446	0.0000	0.51166	0.00003	0.34839	0.00002	0.51141	-2.7
SQ13-110-4	6.0	0.0444	0.0001	0.51165	0.00003	0.34842	0.00002	0.51141	-2.8
SQ13-110-5	7.1	0.0484	0.0001	0.51170	0.00006	0.34842	0.00005	0.51143	-2.4
SQ13-110-6	7.5	0.0472	0.0000	0.51167	0.00002	0.34840	0.00001	0.51141	-2.9
SQ13-110-7	6.6	0.0477	0.0001	0.51166	0.00003	0.34839	0.00001	0.51140	-3.0
SQ13-110-8	6.4	0.0488	0.0000	0.51169	0.00003	0.34841	0.00002	0.51142	-2.7
SQ13-110-9	6.7	0.0478	0.0000	0.51166	0.00003	0.34842	0.00002	0.51140	-3.1
SQ13-101-1	5.0	0.0444	0.0000	0.51161	0.00004	0.34839	0.00002	0.51137	-3.7
SQ13-101-2	5.6	0.0450	0.0001	0.51164	0.00003	0.34843	0.00002	0.51139	-3.2
SQ13-101-3	5.7	0.0454	0.0000	0.51168	0.00003	0.34840	0.00002	0.51143	-2.4
SQ13-101-4	5.5	0.0440	0.0000	0.51162	0.00003	0.34841	0.00002	0.51138	-3.4
SQ13-101-5	7.4	0.0457	0.0000	0.51168	0.00002	0.34842	0.00001	0.51143	-2.4
SQ13-101-6	7.6	0.0468	0.0000	0.51169	0.00003	0.34844	0.00002	0.51143	-2.5
SQ13-101-7	4.5	0.0433	0.0000	0.51159	0.00004	0.34843	0.00002	0.51135	-4.0
SQ13-101-8	5.7	0.0408	0.0000	0.51165	0.00003	0.34842	0.00002	0.51143	-2.5
SQ14-16-1	4.0	0.0377	0.0000	0.51158	0.00003	0.34836	0.00002	0.51137	-3.6
SQ14-16-2	7.5	0.0384	0.0000	0.51160	0.00003	0.34843	0.00002	0.51139	-3.2
SQ14-16-3	8.2	0.0390	0.0000	0.51162	0.00002	0.34841	0.00002	0.51140	-3.0
SQ14-16-4	7.2	0.0367	0.0001	0.51169	0.00009	0.34847	0.00007	0.51148	-1.4
SQ14-16-5	7.9	0.0362	0.0001	0.51167	0.00009	0.34847	0.00006	0.51147	-1.6
SQ14-16-6	8.0	0.0363	0.0001	0.51163	0.00007	0.34843	0.00005	0.51143	-2.4
SQ14-16-7	8.7	0.0369	0.0001	0.51165	0.00004	0.34844	0.00003	0.51145	-2.0
SQ14-16-8	7.4	0.0381	0.0000	0.51163	0.00006	0.34842	0.00004	0.51142	-2.6
SQ14-16-9	7.9	0.0374	0.0000	0.51163	0.00004	0.34842	0.00003	0.51143	-2.5

SQ14-16-10	7.2	0.0371	0.0000	0.51163	0.00003	0.34844	0.00003	0.51143	-2.5

Note: The data for allanite-(Ce) are from Li and Zhou (2017).

Table 5 Bulk-mineral Sm-Nd isotopic composition of fluorapatite

Sample	Sm(ppm)	Nd(ppm)	$^{147}Sm/^{144}Nd$	$^{143}Nd/^{144}Nd$	2σ	$(^{143}Nd/^{144}Nd)_i$	εNd(t=840Ma)
SQ13-96	239.5	1303	0.1111	0.511809	0.000012	0.511197	-7.0
LC11-55	170.8	929.3	0.1112	0.511817	0.000013	0.511205	-6.8
LC11-77	112.9	666.9	0.1024	0.511822	0.000014	0.511258	-5.8